

The baryon content of magnetically arrested black hole disks and jets

Anthony Chow,^{1*} Lorenzo Sironi,^{1,2} Bart Ripperda,^{3,4,5,6} Amir Levinson⁷

¹*Department of Astronomy and Columbia Astrophysics Laboratory, Columbia University, New York, NY 10027, USA*

²*Center for Computational Astrophysics, Flatiron Institute, 162 Fifth Avenue, New York, NY 10010, USA*

³*Canadian Institute for Theoretical Astrophysics, 60 St. George St, Toronto, ON M5S 3H8, Canada*

⁴*Department of Physics, University of Toronto, 60 St. George St, Toronto, ON M5S 1A7, Canada*

⁵*David A. Dunlap Department of Astronomy & Astrophysics, University of Toronto, 50 St. George St, Toronto, ON M5S 3H4, Canada*

⁶*Perimeter Institute for Theoretical Physics, 31 Caroline St. North, Waterloo, ON N2L 2Y5, Canada*

⁷*School of Physics and Astronomy, Tel Aviv University, Tel Aviv 69978, Israel*

Accepted XXX. Received YYY; in original form ZZZ

ABSTRACT

We study the transport of baryons in magnetically arrested accretion flows and relativistic jets using general relativistic magnetohydrodynamic simulations that incorporate a passive Eulerian tracer. The tracer allows us to reconstruct a proxy for the physical baryon density supplied by the accretion disk while excluding the mass injected numerically to maintain stability in highly magnetized, low-density regions. Applying this method to axisymmetric black hole simulations with varying spin, we show that baryon loading of the jet is intrinsically episodic and regulated by magnetic flux eruption cycles occurring in the inner accretion flow. Each eruption evacuates baryons from the innermost equatorial region, drives reconnection in extended current sheets, and expels moderately magnetized disk material along the funnel wall, establishing a recurrent mass-loading channel. In spinning black holes, shear-driven waves along the jet boundary further enhance baryon entrainment, whereas this mechanism is suppressed in the non-spinning case. For parameters representative of the black hole accretion flow in M87, we map the global structure and time evolution of the Goldreich–Julian screening boundary, defined as the surface separating regions where the plasma density is sufficient to supply the charges required to screen electric fields parallel to the magnetic field from regions that are charge starved. For spinning black holes, we find that the electromagnetic power of the jet is predominantly carried by baryon-poor plasma, with extended time intervals of charge starvation. Our results provide a framework for diagnosing jet composition, charge starvation, and reconnection-driven mass loading in magnetically arrested black hole systems, with direct implications for particle acceleration and non-thermal emission in low-luminosity accretion flows.

Key words: accretion, accretion discs – magnetic reconnection – relativistic processes – (magnetohydrodynamics) MHD – plasmas – methods: numerical

1 INTRODUCTION

Relativistic jets are among the most powerful manifestations of black hole activity, playing a fundamental role in both galactic and extragalactic environments (see the reviews by Blandford et al. 2019; Kara & García 2025). They act as efficient channels for feedback, regulating star formation and the thermal state of interstellar and intracluster media (e.g., Fabian 2012). Their broadband, non-thermal emission spans the entire electromagnetic spectrum—from radio to X-ray and γ -ray—and arises from a combination of leptonic and hadronic processes. In addition to their dynamical and radiative output, relativistic jets have been considered potential sites for accelerating ultra-high-energy cosmic rays (UHECRs) and producing high-energy neutrinos (Kotera & Olinto 2011; Rodrigues et al. 2021; Abbasi et al. 2022). Magnetic reconnection in highly magnetized relativistic outflows (Sironi et al. 2025) can efficiently accelerate protons to $\gtrsim 10^{19}$ eV (e.g., Zhang et al. 2021), motivating jet-based proton-

acceleration models. The ~ 290 TeV neutrino detected in coincidence with a gamma-ray flare in the blazar TXS 0506+056 (IceCube Collaboration et al. 2018; Padovani et al. 2018) has demonstrated that jets can be powerful neutrino sources, implying the presence of relativistic protons accelerated to energies beyond the PeV scale.

In addition to relativistic jets, magnetically powered coronal regions near the black hole have recently been proposed as potential neutrino production sites. In fact, the strongest current candidate for a neutrino emitter, NGC 1068 (IceCube Collaboration et al. 2022), shows TeV neutrino emission consistent with originating from the nuclear region, while exhibiting no evidence for a relativistic jet or associated gamma-ray emission (Fischer et al. 2023). These observations favor an X-ray-emitting coronal region—rather than a jet-based scenario—as the origin for TeV neutrinos. In systems reaching the magnetically arrested disk (MAD) state—where accretion advects sufficient poloidal magnetic flux to intermittently suppress mass inflow near the black hole horizon (Narayan et al. 2003; Tchekhovskoy et al. 2011)—flux-eruption-driven reconnection layers forming near the black hole are invoked to be promising sites for proton accelera-

* E-mail: kc3058@columbia.edu

tion (Stathopoulos et al. 2024; Hakobyan et al. 2025) and potentially high-energy neutrino production (Fiorillo et al. 2024; Karavola et al. 2025, 2026) in non-jetted sources.

The composition of relativistic jets — and in particular their baryon loading — plays a central role in shaping both their dynamics and their radiative properties. The amount of baryonic matter (protons and heavier ions) entrained in the relativistic outflow determines the plasma density and inertia of the jet. Since the plasma is approximately charge neutral, the electron density is at least comparable to the ion density. Therefore, the ion number density may be compared to the Goldreich–Julian (GJ) density (Goldreich & Julian 1969), which represents the minimum charge density required to short out the electric fields (parallel to the magnetic field) induced by a rotating magnetosphere, which is a good approximation for the innermost region of the accretion flow (Ripperda et al. 2022; Chael et al. 2023; Wong et al. 2025a). If the plasma density falls below the GJ value, the available charges are insufficient to supply the currents demanded by the magnetospheric field structure. In this charge-starved regime, vacuum gaps inevitably form — regions where strong unscreened electric fields can accelerate particles to ultra-relativistic energies, enabling pair creation and non-thermal emission (Hirotani & Okamoto 1998; Hirotani et al. 2017; Levinson & Cerutti 2018; Crinquand et al. 2020; Yuan et al. 2025). On the other hand, if the plasma density is much higher than the GJ density, the magnetosphere remains well-screened, and the presence of baryons (as opposed to a pure electron–positron plasma) increases the inertia of the flow. The degree of baryon loading determines the maximum attainable Lorentz factor of the jet (Toma & Takahara 2012; Sikora & Madejski 2000; Levinson 2000; Cerruti 2020; Kantzas et al. 2023).

Beyond its dynamical role, plasma composition has important implications for the radiative signatures of black hole systems. In sources approaching the MAD state, the jet base and inner magnetosphere become highly magnetised, enabling magnetic pressure to drive violent flux eruptions (Ripperda et al. 2022) and to form reconnecting current sheets. These reconnection layers are promising sites for proton acceleration up to ultra-high energies in low-luminosity sources (Stathopoulos et al. 2024). The baryon content of these layers also regulates the efficiency and observational relevance of proton synchrotron emission. As shown by Hakobyan et al. (2025), proton synchrotron can still be energetically important even when protons are subdominant in number and mass density; for the plasma conditions expected in M87, protons can tap a significant fraction of the dissipated magnetic energy and dominate the emission in the GeV band during flux eruptions. Thus, a proper assessment of baryon loading within MAD reconnection layers is essential for evaluating their potential as proton accelerators and for understanding the radiative signatures of low-luminosity accreting systems.

Plasma composition also influences the radiative properties of relativistic jet boundary layers or sheaths, where dissipation and mixing are expected to be significant. Dissipation associated with jet boundary layers has been observed in the form of limb-brightened radio emission (Janssen et al. 2021). The jet boundary layer has also been proposed as a potential candidate for the X-ray Comptonising corona in luminous sources (Sridhar et al. 2025). In this scenario, the optical depth to Compton scattering depends sensitively on whether the plasma at the jet boundary is baryon- or pair-dominated. Constraining the baryon content at jet boundaries is therefore critical for interpreting coronal or jet boundary emission, motivating future global simulations of black hole accretion flows with self-consistent electron thermodynamics and proper radiation physics.

In summary, accurately constraining the baryon content of magnetically dominated black hole environments is essential not only for

understanding their global electrodynamics — such as gap formation — but also for assessing their mass loading and their ability to act as high-energy particle accelerators and as sources of non-thermal radiation and high-energy neutrinos.

The set of equations of general relativistic magnetohydrodynamics (GRMHD), which evolve the plasma mass, momentum and energy densities as well as the magnetic field in curved spacetimes, provides the primary framework for studying black hole accretion and jet dynamics (Gammie et al. 2003; McKinney 2006; Porth et al. 2017). However, GRMHD methods have intrinsic limitations—particularly in low-density, magnetically dominated regions, such as the jet, the black hole magnetosphere, and the reconnection layers created by flux eruptions. To maintain numerical stability, such methods impose upper limits on the plasma magnetization (i.e., on the ratio of magnetic field enthalpy density to plasma enthalpy density) and enforce density floors by continuously injecting mass in regions where the plasma density would otherwise fall below a prescribed minimum. In typical setups, the accretion disk is initialized with a physically motivated magnetization and genuine baryonic matter, while the surrounding atmosphere and jet regions are initialized with an *ad hoc* maximum magnetization and a corresponding *ad hoc* minimum density. As the simulation evolves, the persistent mass injection required to maintain numerical stability erases information about the physical density and plasma content in low-density, magnetically dominated regions. Consequently, such numerical prescriptions, though essential for stability, mask the physical baryon loading and composition in the magnetosphere and the jet.

Recent work by Wong et al. (2021); Wong et al. (2025b) employed 3D GRMHD simulations of MAD to investigate baryon loading at the jet boundary. They considered a retrograde disk and identified the disk–jet interface by the sign reversal of the azimuthal four-velocity (u_ϕ). To track the transport of matter across this interface, they implemented a passive tracer method, in which Lagrangian particles are initialized with probabilities proportional to the local mass density in the initial disk, and they are advected according to the local fluid velocity. This approach allowed them to follow individual tracer particles through space and time, capturing the entrainment of disk material into the jet. By analyzing when the tracer particles’ radial and azimuthal velocities changed sign, Wong et al. (2021) identified the onset of disk-to-jet mass entrainment and suggested that these episodic mass-loading events arise from Kelvin–Helmholtz (KH) instabilities developing along the jet boundary layer (Chow et al. 2023; Davelaar et al. 2023).

In this study, we adopt a different approach. Rather than using discrete Lagrangian tracer particles, we employ a passive Eulerian tracer field that records the physical baryon rest-mass density of the accretion flow, independent of the mass added *ad hoc* to maintain the imposed density floors. We initialize the tracer field so that it traces only baryonic material originating from the accretion flow (i.e., it is initialized as zero outside the disk). The tracer is passively advected with the fluid, and in regions where numerical density floors inject matter, its value is adjusted so that the local tracer mass density remains conserved. In this way, the tracer behaves as a strictly passive scalar—carrying no dynamical influence—which faithfully tracks the transport of disk-supplied baryons throughout the simulation. This allows us to separate genuine baryonic material supplied by the accretion flow from mass that is numerically injected through density floors—the latter would likely be dominated by electron–positron pairs. This enables us to follow the transport of disk material into the black hole magnetosphere and jet funnel. We perform axisymmetric (2D) ideal GRMHD simulations of MADs around black holes with three different spins—prograde (with respect to the disk angular mo-

mentum), non-spinning, and retrograde—to focus on the dynamics of mass transport and baryonic loading.

We note that all simulations presented in this work are performed in axisymmetry (2D), which imposes well-known limitations. In particular, axisymmetric calculations do not sustain long-lived magnetorotational turbulence, and the turbulent cascade to small scales is suppressed. As a result, some aspects of angular-momentum transport are not captured in a fully realistic manner. However, in the MAD regime, the global dynamics is dominated by large-scale, coherent magnetic fields rather than by small-scale turbulence. Phenomena central to the MAD state—such as the accumulation of poloidal magnetic flux near the black hole, episodic magnetic-flux eruptions, large-scale reconnection events, and the formation of a strongly magnetized funnel—can be qualitatively captured in axisymmetric simulations (Ripperda et al. 2020). We acknowledge, however, that non-axisymmetric modes may drive interchange instabilities in the inner magnetosphere, and thus modify some of the conclusions of this work, as we also discuss in §4.5.

This paper is organized as follows. In §2, we present the method of using a passive Eulerian tracer to reconstruct the physical baryon density field. §3 describes the numerical setup of the MAD accretion flow simulations and the GRMHD code used in our study. §4 contains our main findings: §4.1 examines how flux-eruption cycles regulate the accretion rate of baryonic matter; §4.2 analyzes how black-hole spin affects the structure and dynamics of the baryon magnetization (hereafter, the tracer magnetization, which we define as the ratio of magnetic enthalpy density to baryonic rest-mass energy density), in the course of individual eruption events; §4.3 studies the baryon loading near the equatorial current sheet; §4.4 illustrates the geometry of the Goldreich–Julian screening boundary, which governs where and when charge starvation occurs in the jet, for parameters representative of the black hole accretion flow in M87; and §4.5 quantifies the degree of baryonic mass loading of the jet, by partitioning the jet electromagnetic power by tracer magnetization. §5 summarizes our conclusions and discusses the implications of our results for jet dynamics and non-thermal emission.

2 IMPLEMENTATION OF THE BARYON TRACER DENSITY

The primary aim of this work is to investigate the baryon loading of the highly magnetized jet and magnetosphere of the black hole. We employ the GRMHD code BHAC (Porth et al. 2017; Olivares et al. 2019), which regulates the maximum plasma magnetization through the injection of density floors. The code imposes a maximum value of the cold magnetization,

$$\sigma_{\max} = \frac{b^2}{4\pi c^2 \rho_{\text{floor}}}, \quad (1)$$

where b is the co-moving magnetic field. Mass injection is activated when the cold magnetization exceeds some prescribed $\sigma_{\max} = 100$. By injecting floor density, ρ_{floor} , the code enforces $\sigma < \sigma_{\max}$ and maintains numerical stability in magnetically dominated regions. This artificial mass injection, however, limits our ability to recover the physical baryon density in highly magnetized regions. To address this, we make use of a passive scalar tracer.

A passive tracer χ_{tr} is a quantity that is advected with the fluid flow but does not influence the system’s dynamics (Porth et al. 2014). For the sake of comparison, the evolution of the mass density ρ is governed by the mass continuity equation

$$\nabla_{\mu}(\rho u^{\mu}) = 0, \quad (2)$$

where u^{μ} is the fluid 4-velocity and Greek indices $\mu = 0, 1, 2, 3$ denote spacetime components, with ∇_{μ} the covariant derivative associated with the spacetime metric. The tracer density $\rho_{\text{tr}} = \rho \chi_{\text{tr}}$ evolves according to the tracer continuity equation

$$\nabla_{\mu}(\rho_{\text{tr}} u^{\mu}) = 0, \quad (3)$$

i.e., it is advected with the same four-velocity u^{μ} as the MHD fluid. The evolution of energy and momentum of the MHD fluid depend only on Equation (2) and not on Equation (3). This implicitly requires that the global dynamics is nearly independent of the value chosen for σ_{\max} . In Appendix A, we verify that our results do not depend on the maximum magnetization σ_{\max} . The tracer field is inevitably subject to numerical diffusion; we assess the degree of numerical convergence with respect to grid resolution in Appendix B.

For the purposes of this study, we interpret ρ_{tr} as a proxy for the baryon mass density unaffected by the injection of density floors. To preserve the value of the tracer density when floor mass is injected, the updated tracer fraction (i.e., the tracer fraction $\chi_{\text{tr}}^{\text{new}}$ after floor injection) must satisfy

$$\rho_{\text{floor}} \chi_{\text{tr}}^{\text{new}} = \rho \chi_{\text{tr}}. \quad (4)$$

This essentially states that the tracer mass density ρ_{tr} is unaffected by the addition of density floors.

At the start of the simulation, we initialize the passive tracer fraction to tag matter originating in the disk by setting $\chi_{\text{tr}} = 1$ inside the accretion disk and $\chi_{\text{tr}} = 0$ in the ambient medium. Interpreting the tracer as a proxy for baryonic mass, this choice allows us to track the transport and redistribution of baryons originating from the disk into the whole domain, including magnetically dominated regions.

3 NUMERICAL SETUP

This work employs axisymmetric ideal GRMHD simulations performed with BHAC in a logarithmic Kerr-Schild coordinate system (McKinney & Gammie 2004), with t representing time and r, θ, ϕ the radial, polar, and toroidal coordinates (for a logarithmic Kerr-Schild metric, the radial coordinate is $\log r$). We investigate MAD configurations with three representative values of the dimensionless spin parameter, $a \in [-0.9375, 0, 0.9375]$, corresponding respectively to near-extremal retrograde Kerr, Schwarzschild, and near-extremal prograde Kerr black holes.

With the gravitational radius defined as $r_g = GM_{\bullet}/c^2$, where M_{\bullet} is the black hole mass, we measure lengths and times in units of r_g and r_g/c , respectively. We also adopt the Lorentz-Heaviside units, where a factor of $1/\sqrt{4\pi}$ is absorbed into the electromagnetic fields. Each simulation is initialized with a hydrodynamic equilibrium torus (Fishbone & Moncrief 1976) threaded by a single weak poloidal magnetic field loop, defined through the vector potential

$$A_{\phi} \propto \max(q, 0), \quad (5)$$

where

$$q = \frac{\rho}{\rho_*} \left(\frac{r}{r_{\text{in}}} \right)^3 \sin^3 \theta \cdot \exp\left(-\frac{r}{400 r_g}\right) - 0.2, \quad (6)$$

with an inner radius $r_{\text{in}} = 20 r_g$ and a density maximum ρ_* located at r_{max} . To enable a consistent comparison across simulations with different spins, we adopt $r_{\text{max}} = 41 r_g, 41.4 r_g$ and $42 r_g$ for $a = 0.9375, 0, -0.9375$, respectively. These choices of r_{max} ensure that the disks have comparable sizes for the three different spins.

The initial magnetic field strength is normalized such that the plasma beta $2p/b^2 = 100$, where p denotes the plasma pressure.

We set an atmospheric rest-mass density $\rho_{\text{atm}} = \rho_{\text{min}}(r/r_g)^{-3/2}$ and pressure $p_{\text{atm}} = p_{\text{min}}(r/r_g)^{-5/2}$, where $\rho_{\text{min}} = 10^{-4}$ and $p_{\text{min}} = 10^{-6}/3$, as in Ripperda et al. (2020). In the course of the evolution, we apply floors on rest-mass density, pressure, and Lorentz factor $\Gamma < \Gamma_{\text{max}} = 20$, and we maintain a cold magnetization $\sigma = b^2/\rho c^2 < \sigma_{\text{max}} = 100$ and plasma beta $\beta = 2p/b^2 > \beta_{\text{min}} = 1/(10\sigma_{\text{max}})^{(\hat{\gamma}-1)}$, where $\hat{\gamma}$ is the adiabatic index. We employ the equation of state of a relativistic ideal gas with $\hat{\gamma} = 4/3$.

The magnetorotational instability (Velikhov 1959; Chandrasekhar 1960; Balbus & Hawley 1991) is triggered by perturbing the equilibrium pressure as $p = p_{\text{eq}}(1 + X_p)$, where p_{eq} is the analytic equilibrium pressure of the Fishbone–Moncrief torus, and X_p is a uniformly distributed random variable in the range $[-0.02, 0.02]$.

The base grid resolution is 384×192 cells in $(\log r, \theta)$, and the simulations employ five levels of adaptive mesh refinement (AMR), yielding an effective resolution of 6144 radial and 3072 polar cells. We performed a resolution-convergence study to verify the robustness of our results; details are provided in Appendix B.

4 RESULTS

4.1 Temporal evolution of baryon accretion rates

In MADs, magnetic flux eruptions intermittently generate strongly magnetized, low-density regions near the event horizon. These magnetically dominated regions trigger the injection of numerical density floors, causing the total accretion rate to deviate from the physical baryon accretion rate. In this section, we examine how black-hole spin affects the near-horizon accretion dynamics.

Fig. 1 shows the time evolution of the mass accretion rates and of the magnetic flux evaluated on the event horizon. For a Kerr black hole, the outer horizon lies at

$$r_+ = r_g \left(1 + \sqrt{1 - a^2}\right), \quad (7)$$

giving $r_+/r_g = 1.35, 2, 1.35$ for spins $a = 0.9375, 0, -0.9375$, respectively. Let u^r and B^r denote the radial components of the four-velocity and magnetic field, respectively. Then the mass accretion rate (red dashed lines in Fig. 1) is defined as

$$\dot{M} = -2\pi \int_0^\pi \rho u^r \sqrt{-g} \, d\theta, \quad (8)$$

while the tracer mass accretion rate (green solid lines) is

$$\dot{M}_{\text{tr}} = -2\pi \int_0^\pi \rho_{\text{tr}} u^r \sqrt{-g} \, d\theta. \quad (9)$$

The magnetic flux threading the horizon (blue solid lines) is

$$\Phi = \pi \int_0^\pi |B^r| \sqrt{-g} \, d\theta. \quad (10)$$

Following an initial transient phase during which the magnetorotational instability grows and accretion is established, we begin our analysis once the system has reached a quasi-steady state, as indicated by the fact that the mass accretion rate attains a nearly-constant value prior to the onset of magnetic flux eruptions. In prograde accretion (top panel), the time evolution of the magnetic flux from $t \approx 3000 r_g/c$ to $t \approx 5000 r_g/c$ is characterized by small, episodic flux eruptions. After $t \approx 5000 r_g/c$, the eruptions become stronger, produce deeper flux-suppression episodes, and persist for longer durations, although this late-time evolution may be influenced by the assumption of axisymmetry and should be confirmed with fully

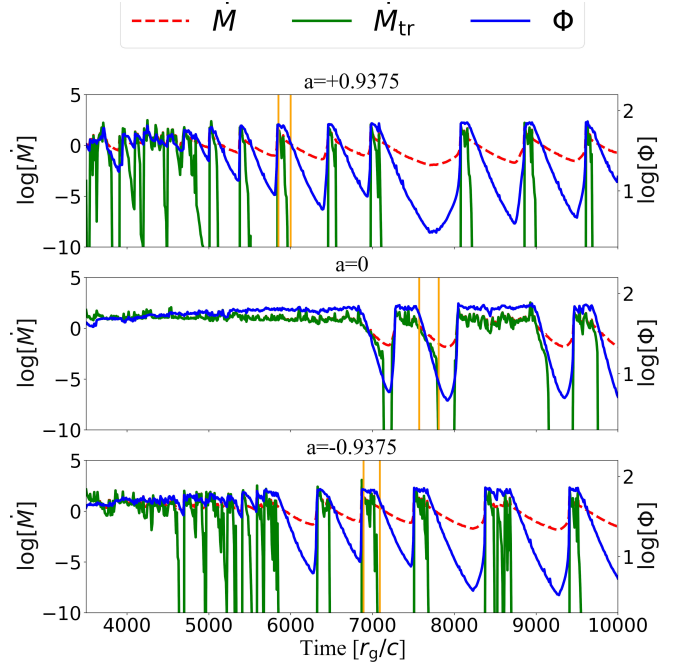


Figure 1. Time evolution of the mass accretion rate \dot{M} (red dashed line), the tracer mass accretion rate \dot{M}_{tr} (green line) and the magnetic flux Φ threading the horizon (blue line) for spin parameter $a = 0.9375$ (top panel), $a = 0$ (middle panel) and $a = -0.9375$ (bottom panel). \dot{M} , \dot{M}_{tr} and Φ are all in code units.

three-dimensional simulations. A similar behavior is observed in retrograde accretion (bottom panel), with flux eruptions of comparable durations and magnitudes as in the prograde case.

In contrast, for the non-spinning case (middle panel), no small-scale flux eruptions are present at early times ($t < 6700 r_g/c$), and large-scale eruptions appear only at later times, after $t \approx 6700 r_g/c$. This delayed onset arises because, in the absence of black-hole spin, frame dragging does not contribute to twisting field lines near the horizon (which would amplify the toroidal field, increasing the overall field strength), and the magnetospheric configuration evolves more slowly toward a highly pressured state. Continued accretion leads to a gradual accumulation of poloidal flux in the funnel region, eventually producing a large-scale flux eruption.

Flux eruptions are accompanied by the formation of magnetospheric reconnection layers (e.g., Ripperda et al. 2020). As accretion drags large-scale poloidal magnetic fields into the black hole, the magnetic pressure at the funnel base accumulates until it becomes comparable to the inflow’s ram pressure. At this point, oppositely directed field lines in the inner disk reconnect violently, producing a flux eruption. This rapid reconfiguration of the magnetic topology drives plasma outward along the reconnected field lines, evacuating the innermost region. As plasma is expelled during the eruption, the density in the vicinity of the black hole drops sharply, giving rise to a magnetically dominated cavity, i.e., a magnetosphere.

During flux eruptions, the drop in density in the inner region is reflected by the decline in the mass accretion rate \dot{M} (red dashed line) and the tracer mass accretion rate \dot{M}_{tr} (green solid line) for all spin cases. Because the magnetization near the black hole often reaches the maximum σ_{max} , numerical floor mass is injected. This explains the divergence between \dot{M} and \dot{M}_{tr} during flux eruptions, with \dot{M}_{tr} dropping much faster. In fact, Fig. 1 demonstrates that most of the mass accreted during flux eruptions comes from numerical floors.

Near the end of a flux eruption, ram pressure begins to dominate over magnetic pressure, allowing baryonic matter to accrete onto the black hole again (in fully three-dimensional systems, this picture may be modified by magnetic interchange instabilities, see Ripperda et al. 2022). Consequently, the divergence between the total mass accretion rate \dot{M} and the tracer accretion rate \dot{M}_{tr} is reduced during phases of high accretion in between consecutive flux eruptions, as the inflow advects baryons back from the disk and the inner accretion channel remains well below the maximum magnetization σ_{max} .

4.2 Baryon dynamics during a single flux-eruption cycle

In this section, we focus on a single eruption cycle and we characterize the evolution of the baryon content at the jet boundary and in the inner equatorial region. We highlight the similarities that emerge among the two rotating black-hole models and the contrasting behaviour of the non-rotating case. Using our passive-tracer modeling of baryons originating in the disk, we identify the physical processes that govern baryon entrainment within the jet funnel.

For a cold plasma, the tracer magnetization is defined as

$$\sigma_{\text{tr}} = \frac{b^2}{\rho_{\text{tr}} c^2} = \frac{b^2}{\rho \chi_{\text{tr}} c^2}, \quad (11)$$

which has the advantage of being insensitive to the magnetization ceiling σ_{max} . Figs. 2-4 present the spatial structure of σ_{tr} obtained from our simulations with spin parameter of $a = 0.9375, 0, -0.9375$ respectively (the corresponding plots for χ_{tr} are displayed in Appendix E) The top row panels display the profile of σ_{tr} over the spatial domain $x = [0, 60] r_g$ and $z = [-10, 70] r_g$ while the bottom row provides a zoomed-in view of the inner region, $x = [0, 15] r_g$ and $z = [-5, 15] r_g$. We focus on the upper hemisphere, as both hemispheres are statistically equivalent. Each column in the figure corresponds to a different simulation time, with $t = [5850, 5900, 5950, 6000] r_g/c$ for the prograde case, $t = [7570, 7640, 7770, 7810] r_g/c$ for Schwarzschild and $t = [6890, 6940, 7040, 7090] r_g/c$ for the retrograde case. These time snapshots are selected to illustrate the temporal evolution of σ_{tr} from the early phase of a magnetic flux eruption (the first orange vertical line in Fig. 1) to the stage when the tracer accretion rate approaches zero (the second orange vertical line in Fig. 1). Figs. 2-4 are also overlaid with magnetic field streamlines (grey lines).

For both the prograde (Fig. 2) and the retrograde case (Fig. 4), panel [a] shows that the jet boundary prior to the flux eruption is laminar, and the tracer magnetization σ_{tr} increases sharply across a very thin layer, from $\sigma_{\text{tr}} \sim 10$ (green) up to 10^6 (white). At this time, the system is accreting in a non-erupting state.

During the initial phase of a flux eruption, reconnection between oppositely oriented magnetic field lines near the equatorial plane gives rise to a baryon-rich, low- σ_{tr} plasmoid chain (panel [f]). At the same time, the magnetic field lines in the jet boundary are perturbed at small radii, and shear-driven vortices (red arrow in panel [b]) develop at the interface between the highly magnetized, low-density white layer and the weakly magnetized, high-density green region. The representative small vortex seen in panel [b] advects outward to larger distances, drawing in ambient baryons as it propagates. As it grows into a larger vortex (red arrow in panel [c]), it leads to further entrainment of low- σ_{tr} baryonic matter into the jet boundary layer.

Later in the eruptive phase (panels [c] and [g]), magnetic field lines that were initially loaded with baryon-rich disk material are now threading the black hole, and their baryonic matter starts flowing out along the jet boundary. On such field lines, baryons can no longer be replenished from the disk, leading to a reduction in the local tracer

density and a corresponding increase in σ_{tr} (see the evolution from green to white at the jet boundary between panels [f] and [g]).

Towards the end of the flux eruption (panels [d] and [h]), the inner region becomes baryon-depleted (panel [h]). In this phase, the equatorial current sheet and its plasmoids are filled primarily with the numerically-injected floor density (in realistic systems, we expect that the layer will be dominated by a pair plasma). Meanwhile, the vortex originating in panel [c] entrains additional baryons as it propagates outward, growing into an even larger vortex (red arrow in panel [d]) that effectively thickens the jet boundary layer.

For the non-rotating black hole case, Fig. 3 corresponds to the second major flux-eruption event as shown by the vertical orange lines in the middle panel of Fig. 1. Compared to prograde and retrograde models, the equatorial reconnection layer is shorter, $\sim 5 r_g$ (panel [h]). Across panels [a]–[d], the disk–funnel interface remains largely laminar throughout the whole duration of the flux-eruption event and exhibits a clear sequence of alternating high- and low- σ_{tr} stripes. We find that this stratification correlates with the sign of the radial plasma velocity (low- σ_{tr} for material coming from the disk towards the black hole, high- σ_{tr} in the opposite case); however, we do not further investigate its physical origin here, since it is likely that three-dimensional effects would smooth or erase such a stratification.

These results show that baryon entrainment within the funnel boundary is governed by two distinct physical processes. First, during the initial baryon-loaded stage of a flux-eruption event, baryons are expelled from the funnel base, thus injecting low- σ_{tr} (i.e., baryon-rich) material directly into the boundary layer, which then propagates to larger radii; this process is present for all three spins, including the non-rotating case. Second, in the rotating black-hole models, shear-driven waves along the jet boundary lead to the formation of vortices as described by Wong et al. (2021), which propagate outward and entrain additional ambient baryons, thereby thickening the mixing layer. No such vortices are observed in the non-spinning model.

4.3 Baryon loading of the equatorial current sheet

The equatorial current sheet that forms during MAD flux eruptions can be a source of bright high-energy emission (Hakobyan et al. 2023). It remains unclear whether reconnection in this layer is fed purely by pair plasma from photon-photon collisions or whether protons originating from the disk also participate. Hakobyan et al. (2025) performed local particle in cell simulations of relativistic reconnection in a pair-proton plasma and demonstrated that even when protons are subdominant in mass and number, they can acquire a sizeable fraction of the dissipated magnetic energy, so their radiative signature (through proton synchrotron emission) can be significant. A reliable quantification of the baryonic content in this region is therefore essential to predict its high-energy signatures. In this subsection, we focus on the innermost magnetospheric region around the current sheet, and use the passive tracer to track its baryon content both in time and polar angle, thereby identifying the composition of the material flowing into the reconnection layer.

Fig. 5 shows the temporal evolution of the tracer magnetization σ_{tr} across polar angle θ at fixed radius $r = 3 r_g$ for three black hole spins: $a = 0.9375$ (top), $a = 0$ (middle) and $a = -0.9375$ (bottom). Throughout the evolution of the prograde and retrograde cases, the regions near the polar axis ($\theta < \pi/4$ and $\theta > 3\pi/4$) remain persistently high- σ_{tr} , forming the base of the baryon-poor jet core. Closer to the equator, the early evolution ($4000 r_g/c \lesssim t \lesssim 5000 r_g/c$) is characterized by a broad low- σ_{tr} (green) region extended over a wide range of θ around the equatorial plane ($\theta = \pi/2$), produced by steady accretion and intermittently perturbed by small flux-eruption events

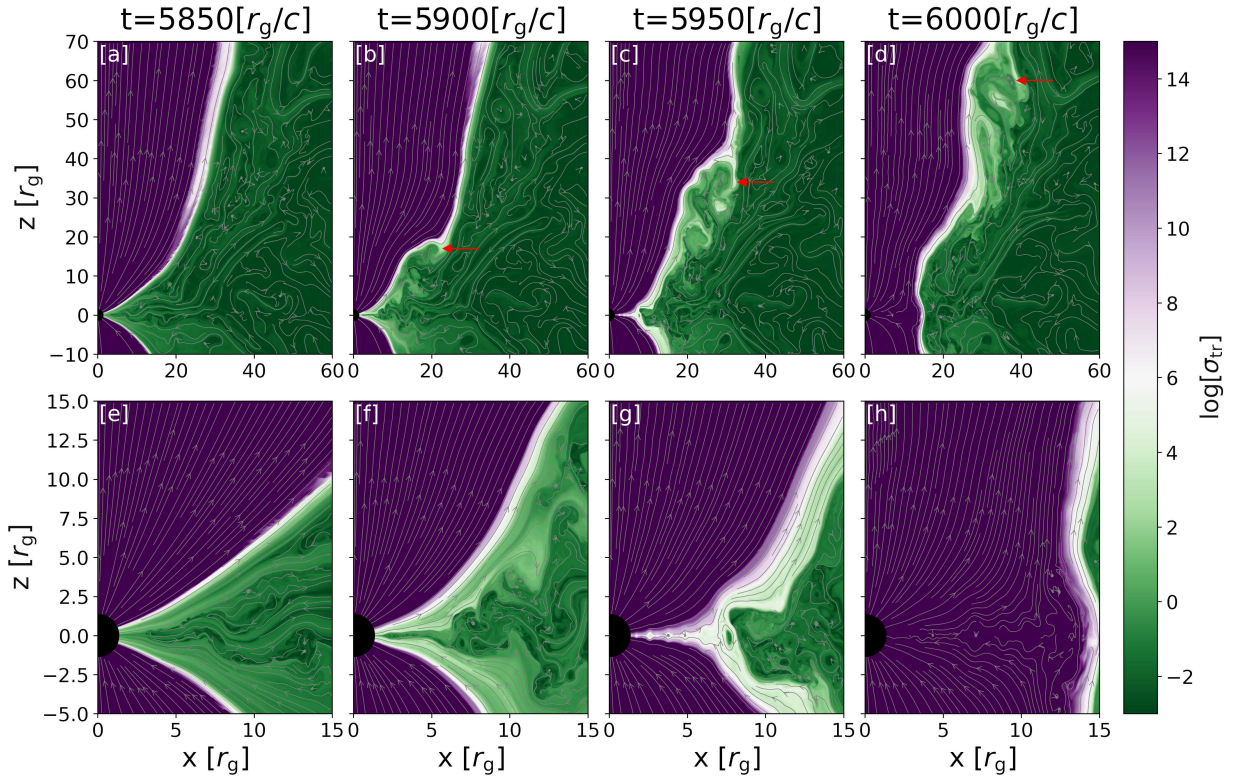


Figure 2. x - z slices of the tracer magnetization, σ_{tr} , at simulation times $t = 5850 r_{\text{g}}/c$, $5900 r_{\text{g}}/c$, $5950 r_{\text{g}}/c$, and $6000 r_{\text{g}}/c$, for a black hole with spin parameter $a = 0.9375$. The upper panels display the large-scale structure, while the lower panels provide a zoomed-in view of the near-horizon region, highlighting the evolution of magnetized outflows and instabilities. Red arrows in panels [b]–[d] point to the location of a growing vortex.

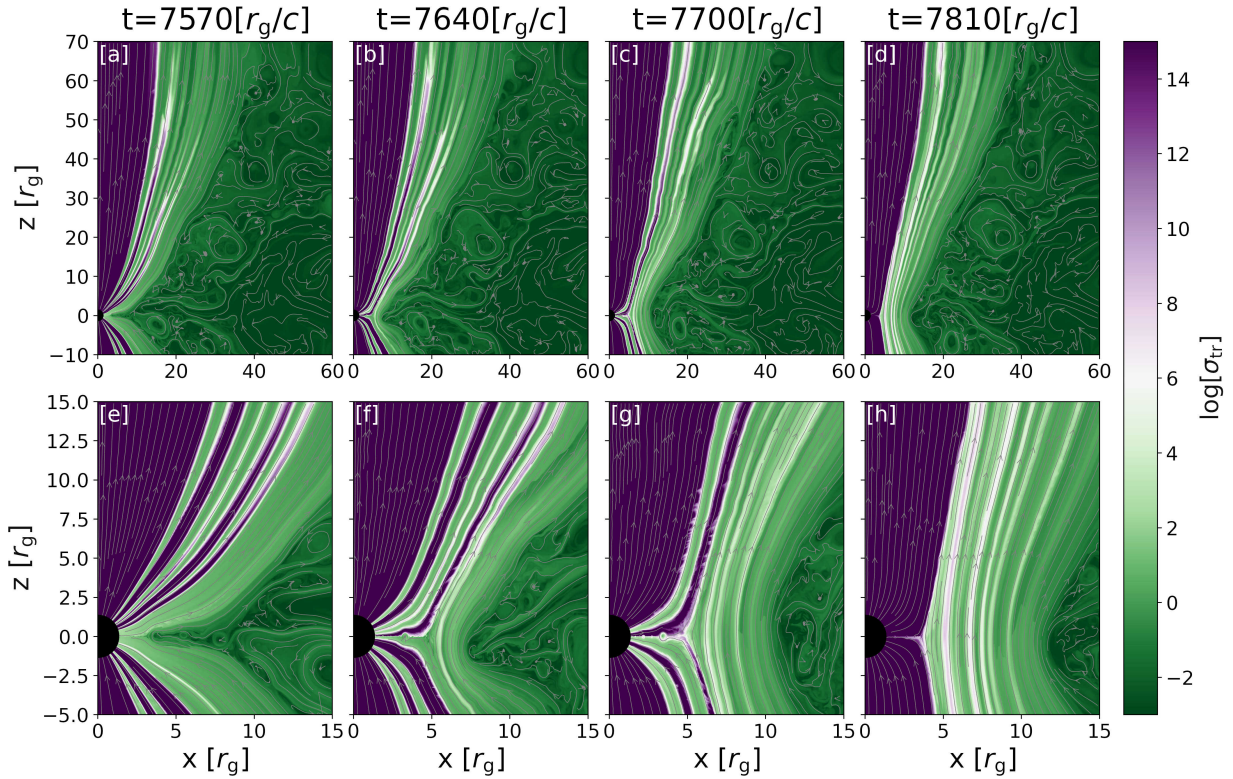


Figure 3. Same as Fig. 2, but for a black hole with spin parameter $a = 0$, shown at simulation times $t = 7570 r_{\text{g}}/c$, $7640 r_{\text{g}}/c$, $7700 r_{\text{g}}/c$, and $7810 r_{\text{g}}/c$.

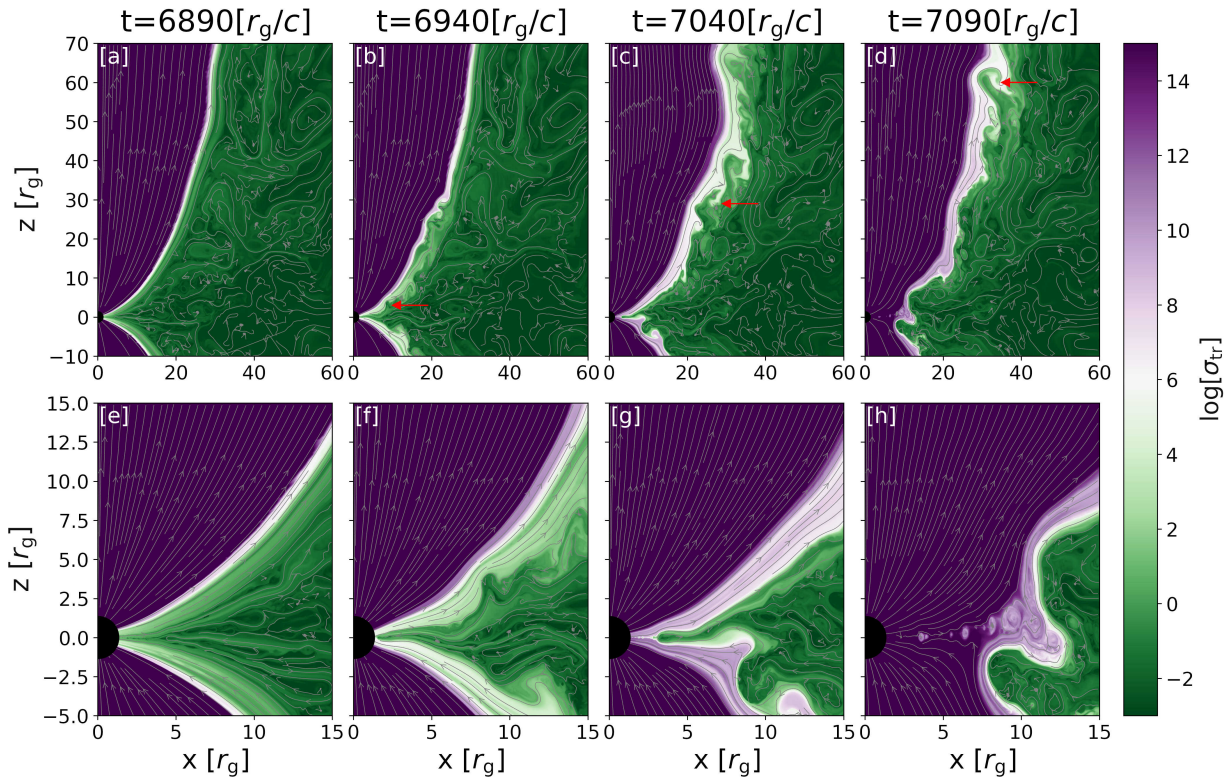


Figure 4. Same as Fig. 2, but for a black hole with spin parameter $a = -0.9375$, shown at simulation times $t = 6890 r_g/c$, $6940 r_g/c$, $7040 r_g/c$, and $7090 r_g/c$.

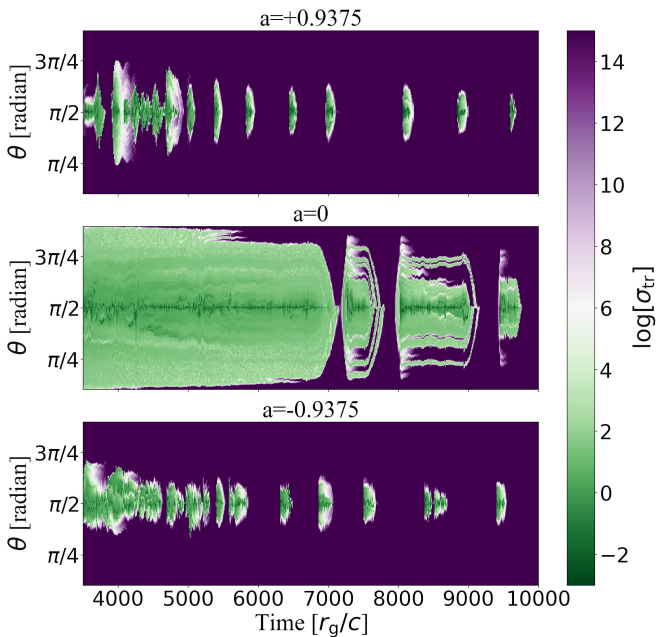


Figure 5. Time evolution of the logarithm of σ_{tr} at different polar angles θ for a fixed radial coordinate $r = 3 r_g$ measured from the center of the black hole. The three panels correspond to different black hole spins: (top) $a = 0.9375$, (middle) $a = 0$, and (bottom) $a = -0.9375$.

(white-purple). These early eruptions reduce—but do not fully remove—the baryon content near the mid-plane. At later times, both rotating models develop a sequence of isolated low- σ_{tr} (green) patches

separated by extended high- σ_{tr} (purple) time intervals. This alternating pattern mirrors the sequence of brief episodes of significant baryon loading during high accretion states followed by baryon depletion during large-scale eruptions. In the course of each eruption, the baryon content at a given polar angle above or below the equator (e.g., take $\theta = 3\pi/8$) is progressively depleted, as marked by the progression from dark green to white and finally purple in Fig. 5. This evolution in σ_{tr} indicates that the plasma flowing into the equatorial current sheet evolves from a baryon-rich to a baryon-poor state in the course of each flux eruption. This can inform hadronic synchrotron emission models, as in the case of the accretion flow in M87 discussed by [Hakobyan et al. \(2025\)](#).

The build-up of magnetic pressure generated by reconnection exhausts during a flux eruption prevents the inflow of disk material and produces extended high- σ_{tr} purple intervals. When the magnetic barrier weakens and accretion resumes, baryon-rich plasma appears as the next low- σ_{tr} green patch. The relatively short duration of the low- σ_{tr} phases is likely a consequence of the axisymmetric nature of the simulations, which suppresses non-axisymmetric magnetic Rayleigh–Taylor-like instabilities that may facilitate sustained accretion in three-dimensional MADs (e.g. [Ripperda et al. 2022](#)).

The behavior of the non-spinning model sharply contrasts with the spinning cases. In most of its evolution, the baryon-poor funnel remains narrowly collimated, which permits low- σ_{tr} (green) material to extend up to substantially higher latitudes than in the rotating cases. Flux-eruption activity develops more gradually than in the rotating cases, with significant eruptions emerging only after $t \approx 7000 r_g/c$, consistent with the slower accumulation of magnetic pressure expected in the absence of frame dragging, as we have discussed above. The resulting high- σ_{tr} (purple) intervals are correspondingly shorter than in the spinning models, indicating that the eruptions themselves

are weaker and less capable of sustaining prolonged baryon depletion in the inner magnetosphere.

4.4 Structure and evolution of the Goldreich–Julian screening boundary

The Goldreich–Julian (GJ) density provides a quantitative criterion for assessing whether the local plasma supply is sufficient to screen parallel electric fields and maintain force-free conditions. Using our passive-tracer–based estimate of the baryon density, ρ_{tr} , we identify regions where the plasma content falls below the GJ threshold, thereby mapping the global structure and temporal evolution of the GJ screening boundary. In charge-starved regions where the plasma density falls below the GJ value, gap formation and self-consistent pair creation—processes not captured within the standard GRMHD framework—would be required to restore force-free conditions.

To quantify the structure of the GJ boundary, we measure at each radius the maximum polar angle in the upper hemisphere, $\theta_{\text{max}} \leq \pi/2$, such that all cells with $\theta < \theta_{\text{max}}$ satisfy $\sigma_{\text{tr}} > \sigma_{\text{GJ}} = 10^{10}$. This threshold corresponds to the GJ density for a magnetic field of ~ 100 G at the horizon, appropriate for M87 (see Appendix C). The critical angle θ_{max} therefore traces the outer edge of the charge-starved region in the jet spine and provides a quantitative measure of how its opening angle evolves in response to magnetic-flux eruptions and reconnection events. Fig. 6 presents the time evolution of θ_{max} as a function of radius and time. We consider only the upper hemisphere and show results for three spins: $a = 0.9375$, $a = 0$, and $a = -0.9375$. The colour scale shows $\log(\theta_{\text{max}}/(\pi/2))$, with darker (redder) regions indicating larger values of θ_{max} . The lower hemisphere is statistically symmetric and exhibits similar behaviour.

We first consider the rotating models (top and bottom panels). At large radii ($r > 25 r_g$), θ_{max} decreases with distance, indicating that the charge-starved jet spine becomes progressively more collimated while the jet boundary gets increasingly baryon-loaded as the jet propagates outward. Superimposed on this global trend are slanted striations produced by disturbances launched near the black hole during magnetic-flux eruptions. These disturbances propagate outward along the jet and modulate the angular extent of the GJ boundary.

At small radii ($r < 25 r_g$), intermittent dark-red patches mark episodes in which strong flux eruptions completely evacuate baryons from the inner magnetosphere. The resulting magnetic pressure creates an equatorial cavity, causing θ_{max} to approach $\pi/2$. This indicates that the charge-starved region extends down to the equator (and, by symmetry, across all polar angles). The peak time of each dark-red patch coincides with a minimum in the tracer accretion rate \dot{M}_{tr} and with the maximum radial extent of the equatorial reconnection layer (or, more generally, of the charge-starved magnetosphere). For example, the blue arrow in the top panel of Fig. 6 marks a charge-starved cavity extending to $22.8 r_g$. As accretion resumes, baryons gradually refill the cavity and θ_{max} decreases. This cycle of baryon evacuation, disk displacement, and subsequent refilling reflects the episodic nature of magnetic-flux eruptions and their impact on the extent of the charge-starved region.

In the non-spinning case ($a = 0$), no rotational energy can be extracted from the black hole and no magnetically powered jet is launched. Regions with $\sigma_{\text{tr}} > \sigma_{\text{GJ}}$ still mark charge-starved zones near the polar axis, but these do not correspond to an active jet spine; instead, they form a low-density, magnetically dominated funnel. For an extended period ($t \lesssim 6700 r_g/c$), the inward advection of magnetic flux is insufficient to trigger significant flux eruptions, and the charge-starved polar region remains narrow and steady. As discussed in §4.1, magnetic-flux eruptions can occur even at zero spin once sufficient

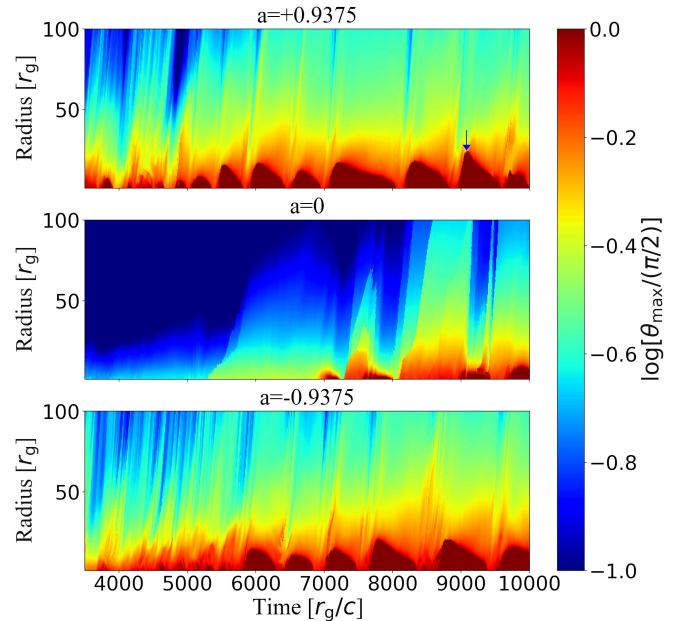


Figure 6. Time–radius diagrams of the maximum polar angle (in radians) in the upper hemisphere ($\theta \leq \pi/2$) at which the tracer magnetization consistently satisfies $\sigma_{\text{tr}} > \sigma_{\text{GJ}} = 10^{10}$. The horizontal axis shows time, and the vertical axis corresponds to radial distance from the black hole, spanning $r \in [0, 100] r_g$. The three panels correspond to different spins: (top) $a = 0.9375$, (middle) $a = 0$, and (bottom) $a = -0.9375$. The blue arrow in the top panel points to the peak of the dark red patch, which corresponds to the maximum extent of the equatorial charge-starved region for $a = 0.9375$.

magnetic flux accumulates in the inner accretion flow. At later times, such eruptions produce the isolated dark-red patches at $\theta_{\text{max}} \approx \pi/2$ in the middle panel of Fig. 6.

4.5 Jet power partitioned by baryonic magnetization

To quantify the degree of baryon loading in the Poynting-dominated jet, we examine how the radial electromagnetic (EM) power is distributed as a function of σ_{tr} . By identifying which magnetization regimes dominate the outward EM energy flux, and how these regimes evolve during flux-eruption episodes, we assess whether the jet remains predominantly charge-starved or becomes sufficiently screened and potentially inertia-dominated. In this subsection we focus on the rotating models and exclude the non-spinning case ($a = 0$), which does not produce a sustained powerful jet.

To quantify how the radial component of the EM power is distributed as a function of the tracer magnetization, let $\partial T_{\text{EM}t}^r / \partial \sigma_{\text{tr}}$ denote the amount of radial EM power carried by plasma of a given magnetization σ_{tr} . We quantify the cumulative electromagnetic power carried by regions with $\sigma_{\text{tr}} < \sigma_{\text{tr},x}$ at radius r and time t by computing

$$L(\sigma_{\text{tr},x}) = 2\pi \int_0^{\sigma_{\text{tr},x}} \int_0^{\pi/2} \frac{\partial T_{\text{EM}t}^r}{\partial \sigma_{\text{tr}}} \sqrt{-g} d\theta d\sigma_{\text{tr}}, \quad (12)$$

where we call $\sigma_{\text{tr},x}$ the tracer magnetization value such that a fraction x of the total radial EM power is carried by plasma with $\sigma_{\text{tr}} < \sigma_{\text{tr},x}$. Equivalently, if we call L_{EM} the total EM power, we define $\sigma_{\text{tr},x}$ such that $L(\sigma_{\text{tr},x})/L_{\text{EM}} = x$. In this subsection, we track the time and radial dependence of $\sigma_{\text{tr},0.25}$ and $\sigma_{\text{tr},0.50}$, and compare them with the GJ magnetization $\sigma_{\text{GJ}} = 10^{10}$ appropriate for M87.

Table 1. Fraction of time (within $t \in [3000, 10000] r_g/c$) for which $\sigma_{\text{tr},0.25}$ and $\sigma_{\text{tr},0.50}$ at radius $r = 80 r_g$ fall below the GJ magnetization $\sigma_{\text{GJ}} = 10^{10}$.

Quantity	Prograde (Fig. 7)	Retrograde (Fig. 8)
$\sigma_{\text{tr},0.25} < \sigma_{\text{GJ}}$	43%	15%
$\sigma_{\text{tr},0.50} < \sigma_{\text{GJ}}$	16%	2%

Fig. 7 summarizes the evolution of the magnetic flux and EM power partition in the prograde case. Panel [a] shows the magnetic flux Φ threading the black hole horizon (see also Fig. 1), while panel [b] displays the total EM energy flux L_{EM} measured at $r = 20 r_g, 40 r_g, 80 r_g$, and $160 r_g$ (see legend). The two quantities are well correlated: during flux accumulation, magnetic flux is advected onto the horizon, strengthening the Blandford–Znajek (BZ) outflow; during flux-eruption episodes, the horizon-threading flux decreases, reducing the jet power. Panels [c] and [d] show the time evolution of $\sigma_{\text{tr},0.25}$ and $\sigma_{\text{tr},0.50}$, respectively, with black dashed horizontal lines marking the characteristic GJ magnetization $\sigma_{\text{GJ}} = 10^{10}$ appropriate for M87 (see §4.4 and Appendix C). The fraction of time for which $\sigma_{\text{tr},0.25}$ and $\sigma_{\text{tr},0.50}$ fall below σ_{GJ} at $r = 80 r_g$ is listed in Table 1. In the prograde model, $\sigma_{\text{tr},0.50} < \sigma_{\text{GJ}}$ for only 16% of the time, while $\sigma_{\text{tr},0.25} < \sigma_{\text{GJ}}$ occurs for 43% of the time. Overall, we find that most of the jet electromagnetic power is carried by baryon-poor plasma with density below the GJ threshold.

Fig. 8 shows the corresponding results for the retrograde case, in the same format as Fig. 7. In this simulation, sub-GJ excursions are even rarer: $\sigma_{\text{tr},0.25} < \sigma_{\text{GJ}}$ occurs only 15% of the time, and $\sigma_{\text{tr},0.50} < \sigma_{\text{GJ}}$ only 2% of the time. This indicates that the retrograde jet remains predominantly charge-starved, with only brief and infrequent episodes of efficient screening. For the retrograde case in Fig. 8, a vertical dashed black line at $t' = t - r/c = 6850 r_g/c$ marks the onset of the increase in magnetic flux (panel [a]) and electromagnetic power (panel [b]) following a flux eruption. The corresponding vertical lines in panels [c] and [d] show that the decrease in $\sigma_{\text{tr},0.25}$ and $\sigma_{\text{tr},0.50}$ occurs simultaneously with the rise in Φ and L_{EM} . This temporal alignment is not unique to this event: similar correlations hold during other eruption events in the same simulation, as well as in the prograde case shown in Fig. 7. Together, these correlations further support the conclusion that flux-eruption events play a key role in regulating the jet mass loading.

5 SUMMARY & DISCUSSION

In this work, we introduce a passive Eulerian tracer that enables reconstruction of the physical baryon density in GRMHD simulations of magnetically arrested accretion flows. By decoupling the evolution of disk-supplied baryons from the mass injected *ad hoc* in highly magnetized, low-density regions, this method reveals the true baryon content of black hole magnetospheres and jets. Applying this framework to axisymmetric simulations of prograde, Schwarzschild, and retrograde black holes, we identify the mechanisms that regulate when, where, and how baryons are entrained from the disk into the jet, providing a quantitative approach to measuring baryon loading in magnetically dominated regions of global GRMHD simulations.

Our simulations show that magnetic-flux-eruption cycles are the primary regulators of baryon loading in the MAD regime. Each eruption expels disk material from the inner equatorial region, producing moderately magnetized, baryon-rich outflows that are advected along the jet boundary. For spinning black holes, shear-driven vortices (Wong et al. 2021) develop near the funnel wall, further entraining

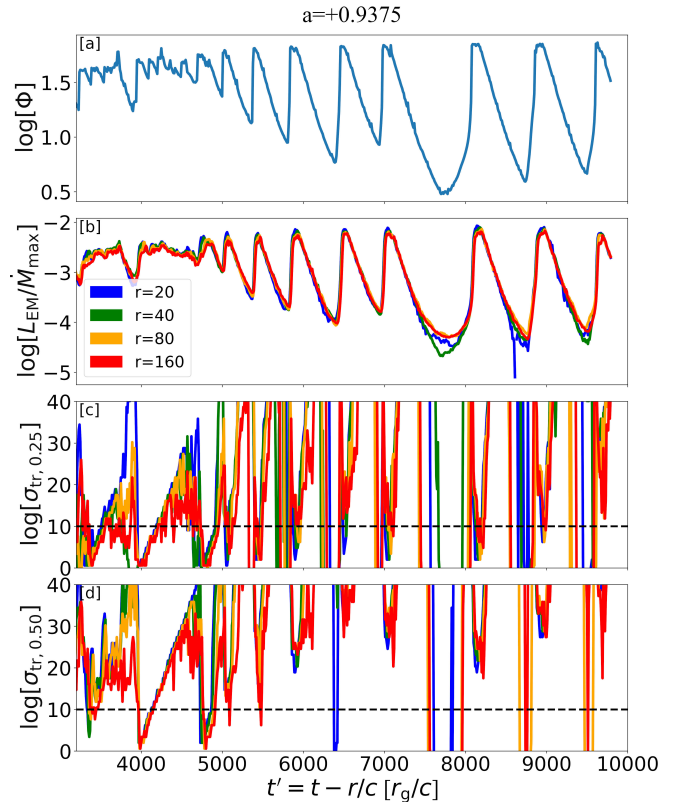


Figure 7. Electromagnetic jet power diagnostics as a function of time for spin $a = 0.9375$. [a] Magnetic flux threading the black hole horizon (same as in Fig. 1). [b] Total radial electromagnetic (EM) power normalized by $M_{\text{max}} c^2$, measured at the radii indicated in the legend. $M_{\text{max}} = 295.82$ is defined as the maximum accretion rate at the event horizon for $t \in [0, 5000] r_g/c$. [c] Tracer magnetization value $\sigma_{\text{tr},0.25}$, defined as the threshold at which 25% of the EM energy flux is carried by material with $\sigma_{\text{tr}} < \sigma_{\text{tr},0.25}$. [d] Tracer magnetization value $\sigma_{\text{tr},0.5}$, corresponding to the median of the EM power distribution. The color scheme for panels (c) and (d) is the same as for panel (b). The black dashed horizontal lines in panels (c) and (d) mark the characteristic GJ magnetization $\sigma_{\text{GJ}} = 10^{10}$ appropriate for M87. Time is shifted in a radius-dependent way to account for light-travel time effects (for panel (a), we take $r = 1.348 r_g$).

disk material and thickening the jet boundary layer; this shear-driven mixing is absent in the non-rotating case.

We also use the passive tracer to quantify the baryon content of the plasma feeding the equatorial current sheet that forms during flux eruptions. We find that the upstream plasma transitions from baryon-rich to baryon-poor over the course of each eruption. This evolution has implications for hadronic emission models powered by pair–proton reconnection, such as those proposed for the accretion flow in M87 (Hakobyan et al. 2025). In this sense, our results provide the global GRMHD context that complements local studies of particle acceleration and nonthermal emission in pair–proton reconnection.

Using the tracer-based baryon density, we map the GJ screening boundary in space and time, identifying where the jet transitions between charge-starved, force-free, and inertia-dominated regimes. Large flux-eruption events temporarily evacuate the inner magnetosphere, extending the charge-starved region—normally confined to the jet funnel—across the full range of polar angles, before accretion gradually refills the cavity. By partitioning the radial electromagnetic jet power by tracer magnetization, we determine whether the

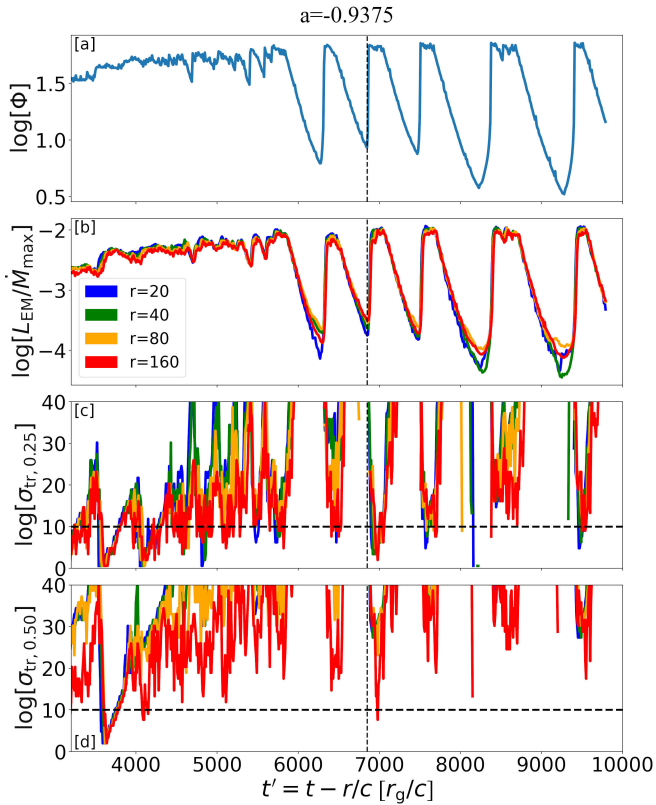


Figure 8. Same as Fig. 7 but for spin parameter $a = -0.9375$. Here, $\dot{M}_{\max} = 196.69$.

Poynting flux is predominantly carried by baryon-rich or baryon-poor plasma. For both prograde and retrograde models, we find that most of the jet electromagnetic power is carried by baryon-poor plasma with density often below the GJ threshold.

Overall, these results show that baryon loading in MAD systems is inherently time-dependent, regulated by eruption-driven ejections from the inner magnetosphere and by turbulent mixing along the jet boundary. The passive tracer introduced here provides a transparent and robust diagnostic of baryon content, jet composition, and charge starvation. It also establishes a framework for future three-dimensional studies, potentially including radiative cooling. Ultimately, this approach will help constrain the jet composition and baryon loading, as well as the radiative signatures of the equatorial current sheet and the jet sheath.

A useful comparison for our results is provided by Wong et al. (2021; Wong et al. 2025b), who studied baryon entrainment in 3D GRMHD simulations using passive Lagrangian tracer particles. They considered a retrograde disk and identified the disk–jet interface through a sign reversal of the azimuthal four-velocity. By tracking particles crossing this interface, they measured a time-averaged entrainment rate of $\sim 0.01\dot{M}$, where \dot{M} is the accretion rate at the horizon, over the interval $t \in [1200, 2000] r_g/c$. Our approach differs, in that we use a passive Eulerian tracer field to reconstruct the physical baryon density. Consistent with Wong et al. (2021); Wong et al. (2025b), we find that baryon entrainment at large radii is dominated by shear-driven mixing associated with vortices developing along the jet boundary. However, one of our main results—that most of the jet electromagnetic power is carried by plasma with density below the GJ threshold—appears at odds with the large entrainment rate reported by Wong et al. (2021).

This discrepancy may arise for several reasons. First, the entrainment rate reported by Wong et al. (2021) is averaged over the interval $t \in [1200, 2000] r_g/c$. In our simulations, this period corresponds to an early evolutionary stage, before the system reaches a quasi-steady state and prior to the onset of large-scale flux eruptions. The resulting time-averaged entrainment rate may therefore not be representative of the MAD regime explored here. In addition, our results indicate that baryon loading in MAD systems is inherently time-dependent and regulated by magnetic-flux–eruption cycles; a time-averaged estimate may therefore miss the intrinsically episodic nature of the entrainment process. Consistent with this interpretation, Fig. 10 of Wong et al. (2021) shows substantial temporal variability in the entrainment rate, which in our framework can be naturally interpreted as a consequence of episodic flux eruptions.

Second, as discussed above, our approach differs from that of Wong et al. (2021) in that we use an Eulerian tracer field rather than Lagrangian tracer particles. In tracer-particle methods such as the AthenaK Lagrangian Monte Carlo scheme (Stone et al. 2024), particles are moved probabilistically between grid cells according to mass fluxes, rather than being strictly advected with the local fluid velocity. This procedure may introduce enhanced diffusion, which could contribute to differences in the inferred entrainment rates. The Eulerian tracer field employed here is itself subject to numerical diffusion; we assess convergence in Appendix B.

Third, the entrainment rate measured by Wong et al. (2021) does not distinguish how deeply tracer particles penetrate into the jet, i.e. whether they reach the region carrying most of the electromagnetic power. Our results could therefore be reconciled with Wong et al. (2021) if most of the baryons entering the jet surface (identified there by the sign reversal of azimuthal four-velocity) remain confined near the jet boundary, while the jet spine—carrying most of the electromagnetic flux—remains baryon-poor. We discuss this possibility further in Appendix D, where we systematically compare our simulations with those of Wong et al. (2021).

Our passive tracer identifies charge-starved regions within the global black-hole accretion–jet system, including both the polar funnel and the innermost equatorial reconnection layer during flux-eruption episodes. In such regions, insufficient charge supply leads to a breakdown of ideal GRMHD and the emergence of unscreened electric fields capable of accelerating particles to ultra-relativistic energies. Charge starvation at the jet base is a persistent feature at all times, including during phases of high accretion; the physics of spindown and subsequent pair creation in the polar region has been studied extensively (e.g., Hirotani et al. 2017; Levinson & Cerutti 2018; Crinquad et al. 2020; Yuan et al. 2025). In contrast, charge starvation in the equatorial current sheet is intrinsically episodic and occurs primarily during the late stages of magnetic flux eruptions. During these episodes, pair creation can supply sufficient plasma to screen the magnetosphere and self-regulate the magnetization of the equatorial current sheet (Hakobyan et al. 2023).

While the passive-tracer framework developed in this work provides a physically transparent assessment of baryon loading in MAD accretion flows, an important limitation is that our study is conducted in axisymmetry. This suppresses inherently three-dimensional instabilities and the associated turbulence that may play a central role in the physics of accretion and mass entrainment. In fully three-dimensional MAD flows, Rayleigh–Taylor-like modes and magnetic interchange instabilities at the disk–magnetosphere interface (Tchekhovskoy et al. 2011; McKinney et al. 2012; Ripperda et al. 2022) enable sustained, non-axisymmetric accretion streams even during eruptive phases, whereas in 2D models magnetic-flux eruptions can temporarily halt accretion. Similarly, mixing and baryon

entrainment at the jet–disk interface may be enhanced by three-dimensional effects (Wong et al. 2021; Davelaar et al. 2023).

Our results show that baryon entrainment and jet mass loading are regulated by the duty cycle and strength of magnetic-flux eruptions—driven by reconnection in the equatorial current sheet—so it is natural to ask how sensitive these processes are to departures from ideal MHD. In ideal GRMHD, reconnection is mediated by numerical resistivity, whereas in resistive GRMHD the reconnection rate and current-sheet structure are controlled by a prescribed conductivity (Komissarov et al. 2007; Ripperda et al. 2020; Grehan et al. 2025). Studies with uniform resistivity indicate that, at sufficiently high resolution, resistive and ideal GRMHD produce similar reconnection behaviour and global dynamics (e.g. Ripperda et al. 2020; Grehan et al. 2025). However, in the reconnection layer of MAD disks—and in many relativistic astrophysical plasmas—the Coulomb mean free path is so large that resistive MHD is formally inapplicable, requiring a kinetic description. In this collisionless regime, particle-in-cell simulations show that reconnection proceeds at rates typically an order of magnitude faster than the asymptotic MHD value (Sironi et al. 2025). Recent work has proposed a kinetically motivated subgrid prescription for non-uniform resistivity (Moran et al. 2025) that reproduces kinetic reconnection rates within MHD simulations. Such a prescription leads to faster reconnection and shorter flux-eruption cycles (Bransgrove et al. 2021; Galishnikova et al. 2023; Ripperda et al. 2026). Systematic comparisons between ideal GRMHD and models incorporating kinetically motivated, non-uniform resistivity will therefore be essential to assess how robust the mass-loading pathways identified here remain once collisionless plasma effects—particularly in reconnection dynamics—are taken into account.

ACKNOWLEDGEMENTS

This work was supported by a grant from the Simons Foundation (MP-SCMPS-00001470). This research was supported in part by grant NSF PHY-2309135 to the Kavli Institute for Theoretical Physics (KITP). L.S. acknowledges support from DoE Early Career Award DE-SC0023015, NASA ATP 80NSSC24K1238, NASA ATP 80NSSC24K1826, NSF AST-2307202, and the Multimessenger Plasma Physics Center (MPPC), grant NSF PHY-2206609. B.R. is supported by grant 23JWGO2A01 from the Canadian Space Agency, and by grants 613413 and RGPIN-2023-04844 from the Natural Sciences and Engineering Research Council of Canada (NSERC).

The computational resources and services used in this work were partially provided by facilities supported by the VSC (Flemish Supercomputer Center), funded by the Research Foundation Flanders (FWO) and the Flemish Government – department EW1, by Compute Ontario and the Digital Research Alliance of Canada (alliancecan.ca) compute allocation rrg-ripperda, and the CCA at the Flatiron Institute supported by the Simons Foundation.

REFERENCES

Abbasi R., et al., 2022, *Phys. Rev. D*, 106, 022005
 Balbus S. A., Hawley J. F., 1991, *ApJ*, 376, 214
 Blandford R., Meier D., Readhead A., 2019, *Annual Review of Astronomy and Astrophysics*, 57, 467
 Bransgrove A., Ripperda B., Philippov A., 2021, *Phys. Rev. Lett.*, 127, 055101
 Cerruti M., 2020, *Galaxies*, 8, 72
 Chael A., Lupsasca A., Wong G. N., Quataert E., 2023, *ApJ*, 958, 65
 Chandrasekhar S., 1960, *Proceedings of the National Academy of Sciences of the United States of America*, 46, 253

Chow A., Davelaar J., Rowan M. E., Sironi L., 2023, *ApJ*, 951, L23
 Crinquad B., Cerutti B., Parfrey K., Philippov A., Dubus G., 2020, *Physical Review Letters*, 124, 145101
 Davelaar J., et al., 2023, *ApJ*, 959, L3
 Fabian A. C., 2012, *Annual Review of Astronomy and Astrophysics*, 50, 455
 Fiorillo D. F. G., Petropoulou M., Comisso L., Peretti E., Sironi L., 2024, *ApJ*, 961, L14
 Fischer T. C., Johnson M. C., Secrest N. J., Crenshaw D. M., Kraemer S. B., 2023, *ApJ*, 953, 87
 Fishbone L. G., Moncrief V., 1976, *ApJ*, 207, 962
 Galishnikova A., Philippov A., Quataert E., Bacchini F., Parfrey K., Ripperda B., 2023, *Phys. Rev. Lett.*, 130, 115201
 Gammie C. F., McKinney J. C., Tóth G., 2003, *The Astrophysical Journal*, 589, 444
 Goldreich P., Julian W. H., 1969, *The Astrophysical Journal*, 157, 869
 Grehan M. P., Ghosal T., Beattie J. R., Ripperda B., Porth O., Bacchini F., 2025, *Physical Review D*, 112
 Hakobyan H., Ripperda B., Philippov A. A., 2023, *ApJ*, 943, L29
 Hakobyan H., Levinson A., Sironi L., Philippov A., Ripperda B., 2025, *ApJ*, 995, L73
 Hirotani K., Okamoto I., 1998, *ApJ*, 497, 563
 Hirotani K., Pu H.-Y., Lin L. C.-C., Kong A. K. H., Matsushita S., Asada K., Chang H.-K., Tam P.-H. T., 2017, *ApJ*, 845, 77
 IceCube Collaboration et al., 2018, *Science*, 361, eaat1378
 IceCube Collaboration Abbasi R., et al. 2022, *Science*, 378, 538
 Janssen M., et al., 2021, *Nature Astronomy*, 5, 1017
 Kantzas D., Markoff S., Lucchini M., Ceccobello C., Chatterjee K., 2023, *MNRAS*, 520, 6017
 Kara E., García J., 2025, *Annual Review of Astronomy and Astrophysics*, 63, 379
 Karavola D., Petropoulou M., Fiorillo D. F. G., Comisso L., Sironi L., 2025, *J. Cosmology Astropart. Phys.*, 2025, 075
 Karavola D., Petropoulou M., Fiorillo D. F. G., Georgakakis A., Comisso L., Sironi L., 2026, arXiv e-prints, p. arXiv:2601.01533
 Komissarov S. S., Barkov M. V., Vlahakis N., Königl A., 2007, *Monthly Notices of the Royal Astronomical Society*, 380, 51
 Kotera K., Olinto A. V., 2011, *Ann. Rev. Astron. Astrophys.*, 49, 119
 Levinson A., 2000, *Phys. Rev. Lett.*, 85, 912
 Levinson A., Cerutti B., 2018, *A&A*, 616, A184
 McKinney J. C., 2006, *Monthly Notices of the Royal Astronomical Society*, 368, 1561
 McKinney J. C., Gammie C. F., 2004, *The Astrophysical Journal*, 611, 977–995
 McKinney J. C., Tchekhovskoy A., Blandford R. D., 2012, *Monthly Notices of the Royal Astronomical Society*, 423, 3083
 Moran A., Sironi L., Levis A., Ripperda B., Most E. R., Selvi S., 2025, *ApJ*, 978, L45
 Narayan R., Igemshchev I. V., Abramowicz M. A., 2003, *Publications of the Astronomical Society of Japan*, 55, L69
 Olivares H., Porth O., Davelaar J., Most E. R., Fromm C. M., Mizuno Y., Younsi Z., Rezzolla L., 2019, *A&A*, 629, A61
 Padovani P., Giommi P., Resconi E., Glauch T., Arsioli B., Sahakyan N., Huber M., 2018, *Monthly Notices of the Royal Astronomical Society*, 480, 192
 Porth O., Xia C., Hendrix T., Moschou S. P., Keppens R., 2014, *The Astrophysical Journal Supplement Series*, 214, 4
 Porth O., Olivares H., Mizuno Y., Younsi Z., Rezzolla L., Moscibrodzka M., Falcke H., Kramer M., 2017, *Computational Astrophysics and Cosmology*, 4, 1
 Ripperda B., Bacchini F., Philippov A. A., 2020, *ApJ*, 900, 100
 Ripperda B., Liska M., Chatterjee K., Musoke G., Philippov A. A., Markoff S. B., Tchekhovskoy A., Younsi Z., 2022, *The Astrophysical Journal Letters*, 924, L32
 Ripperda B., Grehan M. P., Moran A., Selvi S., Sironi L., Philippov A., Bransgrove A., Porth O., 2026, arXiv e-prints, p. arXiv:2601.02460
 Rodrigues X., Heinze J., Palladino A., van Vliet A., Winter W., 2021, *Phys. Rev. Lett.*, 126, 191101
 Sikora M., Madejski G., 2000, *The Astrophysical Journal*, 534, 109

- Sironi L., Uzdensky D. A., Giannios D., 2025, *ARA&A*, **63**, 127
- Sridhar N., Ripperda B., Sironi L., Davelaar J., Beloborodov A. M., 2025, *The Astrophysical Journal*, 979, 199
- Stathopoulos S. I., Petropoulou M., Sironi L., Giannios D., 2024, *Journal of Cosmology and Astroparticle Physics*, p. 009
- Stone J. M., et al., 2024, AthenaK: A Performance-Portable Version of the Athena++ AMR Framework (arXiv:2409.16053), <https://arxiv.org/abs/2409.16053>
- Tchekhovskoy A., Narayan R., McKinney J. C., 2011, *Monthly Notices of the Royal Astronomical Society: Letters*, 418, L79–L83
- Toma K., Takahara F., 2012, *ApJ*, **754**, 148
- Velikhov E. P., 1959, *Soviet Journal of Experimental and Theoretical Physics*, **9**, 995
- Wong G. N., Du Y., Prather B. S., Gammie C. F., 2021, *The Astrophysical Journal*, 914, 55
- Wong G. N., Chael A., Lupsasca A., Quataert E., 2025a, *arXiv e-prints*, p. arXiv:2509.22639
- Wong G. N., Medeiros L., Stone J. M., 2025b, *ApJ*, **995**, 119
- Yuan Y., Chen A. Y., Luepker M., 2025, *ApJ*, **985**, 159
- Zhang H., Sironi L., Giannios D., 2021, *ApJ*, **922**, 261

APPENDIX A: DEPENDENCE ON THE MAGNETIZATION CEILING σ_{\max}

As discussed in §2, GRMHD simulations impose a numerical ceiling σ_{\max} on the magnetization parameter to maintain stability in highly magnetized, low-density regions. Dynamical quantities may therefore, in principle, depend on the adopted magnetization ceiling.

To test the robustness of our results, we perform a parameter study varying $\sigma_{\max} = 25, 50, 100, 200$ in the prograde case. Because mass injection occurs in the most magnetized and least dense regions, any dependence on σ_{\max} should be most evident in the structure of the baryon-depleted jet core. Fig. A1 shows time–radius diagrams of the maximum polar angle θ_{\max} bounding the $\sigma_{\text{tr}} > \sigma_{\text{GJ}} = 10^{10}$ region for each value of σ_{\max} . Despite the factor-of-eight variation in σ_{\max} , all panels display qualitatively similar behaviour, including comparable sequences of flux-eruption events (dark red patches). To quantify these differences further, Fig. A2 shows the evolution of θ_{\max} at fixed radii of $r = 50 r_g$ and $r = 100 r_g$. The curves for all four values of σ_{\max} remain within the same range and show no systematic trend with the magnetization ceiling. We therefore conclude that the system dynamics and tracer-based diagnostics presented here are robust to the adopted value of σ_{\max} .

APPENDIX B: DEPENDENCE ON NUMERICAL RESOLUTION

To assess the numerical convergence of the jet–funnel morphology and baryon loading in our simulations, we performed a resolution study of the prograde case using four grids of increasing resolution: 394×192 -2, 394×192 -3, 394×192 -4, and 394×192 -5. The final digit n denotes the AMR level, where $n = 1$ corresponds to the base grid. Each additional level doubles the resolution in each dimension, yielding effective resolutions of 788×384 ($n = 2$), 1576×768 ($n = 3$), 3152×1536 ($n = 4$), and 6304×3072 ($n = 5$). All simulations were initialized with identical physical and numerical parameters and differ only in the number of AMR levels. The jet funnel is characterized by the maximum polar angle (in radians) in the upper hemisphere ($\theta \leq \pi/2$) for which the tracer magnetization satisfies $\sigma_{\text{tr}} > \sigma_{\text{GJ}} = 10^{10}$. Fig. B1 shows two-dimensional maps of $\log[\theta_{\max}/(\pi/2)]$ as a function of radius and time for the four resolutions. The three highest resolutions (394×192 -5, 394×192 -4, and

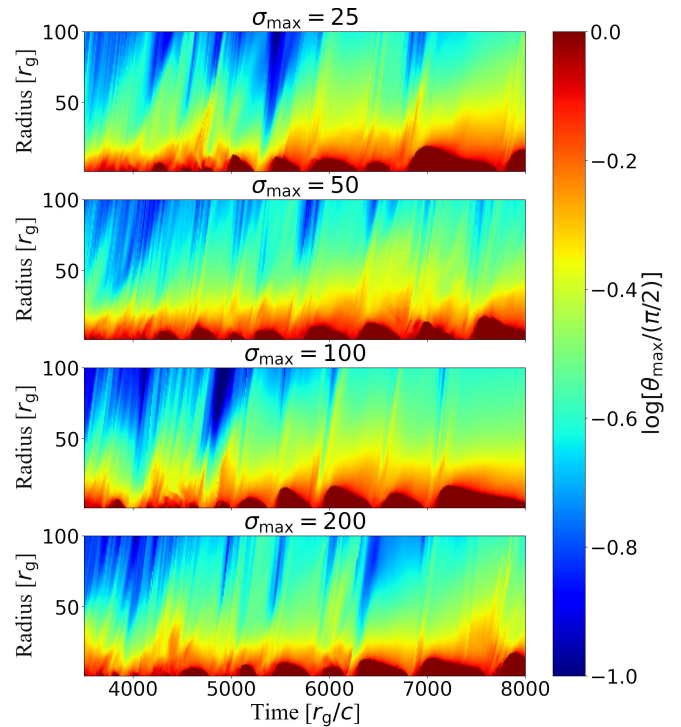


Figure A1. Time–radius diagrams of the maximum polar angle (in radians) in the upper hemisphere ($\theta \leq \pi/2$) at which the tracer magnetization satisfies $\sigma_{\text{tr}} > \sigma_{\text{GJ}} = 10^{10}$. The horizontal axis shows time, and the vertical axis corresponds to radial distance from the black hole, spanning $r \in [0, 100] r_g$. Each panel shows results for a different magnetization ceiling $\sigma_{\max} = 25, 50, 100, 200$.

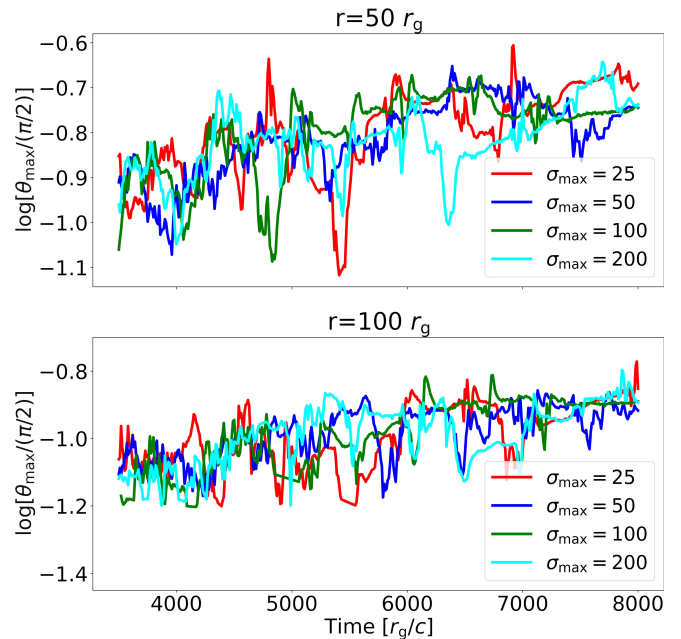


Figure A2. Time evolution of the maximum polar angle θ_{\max} at a fixed radius of $r = 50 r_g$ (top panel) and $r = 100 r_g$ (bottom panel), from the four simulations shown in Fig. A1. The curves show $\log[\theta_{\max}/(\pi/2)]$ for different magnetization ceilings $\sigma_{\max} = 25, 50, 100, 200$ as indicated in the legend. The horizontal axis shows time in units of r_g/c .

394×192-3) exhibit very similar morphologies: the angular extent of the baryon-poor funnel and the time variability of the funnel wall are statistically consistent. This visual agreement indicates that the large-scale geometry of the charge-starved polar region is numerically converged. It also suggests that the flux-eruption dynamics has reached the asymptotic plasmoid-dominated regime of reconnection, in which the reconnection rate is largely independent of numerical resolution (Ripperda et al. 2020; Grehan et al. 2025).

To quantify convergence, Fig. B2 shows θ_{\max} at fixed radii of $r = 50 r_g$ and $r = 100 r_g$. Consistent with Fig. B1, the curves for the three highest resolutions—394×192-5 (red), 394×192-4 (blue), and 394×192-3 (green)—closely track each other throughout the simulation, with only minor deviations. In contrast, the lowest-resolution run, 394×192-2 (cyan), systematically yields smaller values of θ_{\max} than the higher-resolution cases. These results demonstrate that the 394×192-3, 394×192-4, and 394×192-5 grids—the latter adopted in the main body of the paper—have reached convergence for the properties most relevant to this study: (i) the presence and stability of a persistent baryon-depleted jet funnel, (ii) the radial extent of the charge-starved magnetosphere during eruptions, and (iii) the temporal variability of the funnel opening angle. The lowest-resolution run systematically overestimates the baryon loading of the jet funnel, likely due either to enhanced numerical diffusion at the jet–disk boundary or to an artificially elevated reconnection rate when current sheets have not yet reached the asymptotic plasmoid-dominated regime. In the latter case, the higher reconnection rate would promote additional mixing and mass loading, potentially suggesting that the faster reconnection rate ($\sim 0.1 c$) expected in the kinetic regime could further enhance baryon entrainment. Given the agreement between the two highest-resolution cases, we conclude that our fiducial highest-resolution simulation (394×192-5) provides a numerically converged description of the baryon content in the jet and black-hole magnetosphere.

APPENDIX C: THE GOLDBREICH JULIAN DENSITY

In the main body of the paper, we have adopted a representative tracer magnetization threshold of $\sigma_{\text{tr}} = 10^{10}$. This value is motivated by the characteristic GJ magnetization expected in the plasma surrounding a rapidly spinning supermassive black hole such as M87*. This appendix provides the relevant derivations for the GJ number density and the associated magnetization.

The GJ number density is given by

$$n_{\text{GJ}} = \frac{\Omega B}{2\pi e c}, \quad (\text{C1})$$

where e is the elementary charge, c is the speed of light, and Ω is the angular velocity of the black hole magnetosphere, which for near-maximal spin can be approximated by $\Omega \approx c/(2r_g)$. The corresponding GJ magnetization is

$$\sigma_{\text{GJ}} = \frac{B^2}{4\pi m_p c^2 n_{\text{GJ}}} = \frac{eB}{2m_p c \Omega} = \frac{\omega_B}{2\Omega}. \quad (\text{C2})$$

Here m_p is the proton mass and $\omega_B = eB/(m_p c)$ is the proton cyclotron frequency.

Using representative parameters for M87*—gravitational radius $r_g \approx 10^{15}$ cm, angular frequency $\Omega \sim 10^{-5}$ Hz, and magnetic field strength on the horizon $B = 10^2 B_2$ G (Hakobyan et al. 2025)—the estimate for the GJ magnetization is

$$\sigma_{\text{GJ}} \approx 3 \times 10^{10} B_2 \quad (\text{C3})$$

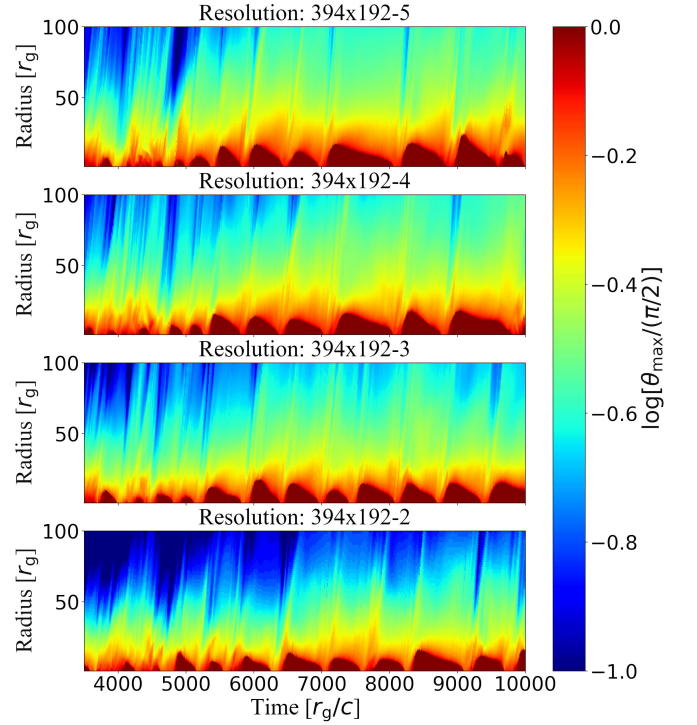


Figure B1. Time–radius diagrams of the maximum polar angle (in radians) in the upper hemisphere ($\theta \leq \pi/2$) at which the tracer magnetization satisfies $\sigma_{\text{tr}} > \sigma_{\text{GJ}} = 10^{10}$. The horizontal axis shows time, and the vertical axis corresponds to radial distance from the black hole, spanning $r \in [0, 100] r_g$. All simulations use the same base grid of 384×192 in $(\log r, \theta)$ -coordinate. The four panels correspond to simulations with different adaptive-mesh-refinement (AMR) levels: from top to bottom, refinement levels 5, 4, 3, and 2, with higher refinement levels providing higher spatial resolution.

This shows that magnetization values of order 10^{10} naturally arise when the plasma density approaches the Goldreich–Julian density in a highly magnetized black-hole magnetosphere with field strengths $B \sim 10^2$ G.

APPENDIX D: COMPARISON WITH EARLIER WORKS

In this appendix, we quantify tracer mass entrainment in the jet using a strategy similar to Wong et al. (2021), with the goal of comparing to their conclusions. We consider the retrograde case and compute the mass outflow rate \dot{M}_{out} in the jet (upper hemisphere only) at different radii (panels from top to bottom in Fig. D1 display $r/r_g = 40, 80$ and 160). The mass outflow rate is calculated using the tracer density, and adopting different definitions for the integration surface, all based on the fact that the jet has negative azimuthal four-velocity ($u_\phi < 0$). In particular, the red line considers all cells up to the maximum polar angle where $u_\phi < 0$ (regardless of the fact that some of these cells may have $u_\phi > 0$; this should be taken as an upper limit for jet opening angle); the green line takes into account all cells up to the minimum angle at which $u_\phi > 0$ (here, all cells have $u_\phi < 0$; this is a lower limit for the jet opening angle); and the blue line only considers cells where $u_\phi < 0$, regardless of whether they are adjacent, or separated by cells with $u_\phi > 0$. Regardless of the specific criterion, the plot confirms that mass entrainment is highly time dependent, and modulated by flux eruption cycles. Comparison

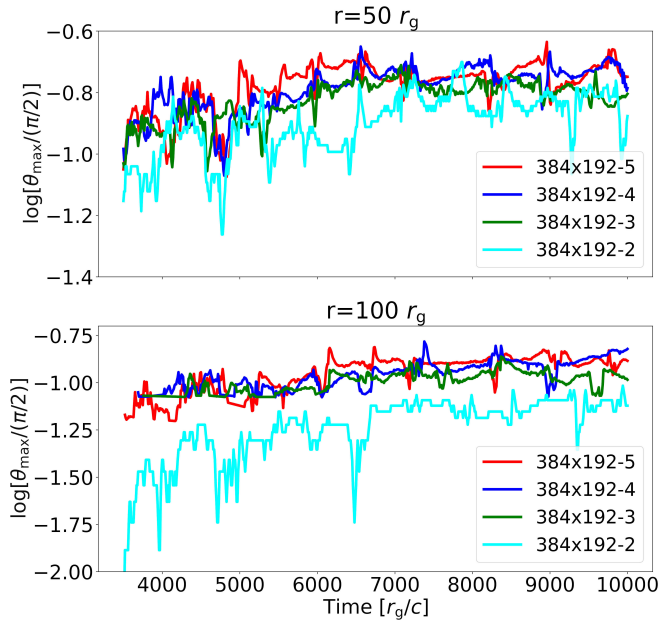


Figure B2. Time evolution of the maximum polar angle θ_{\max} at a fixed radius of $r = 50 r_g$ and $r = 100 r_g$, from the four simulations shown in Fig. B1. The curves show $\log[\theta_{\max}/(\pi/2)]$ for simulations with base grid resolution 384×192 in $(\log r, \theta)$ -coordinates but with different AMR refinement levels: 5,4,3 and 2. The horizontal axis shows time in units of r_g/c .

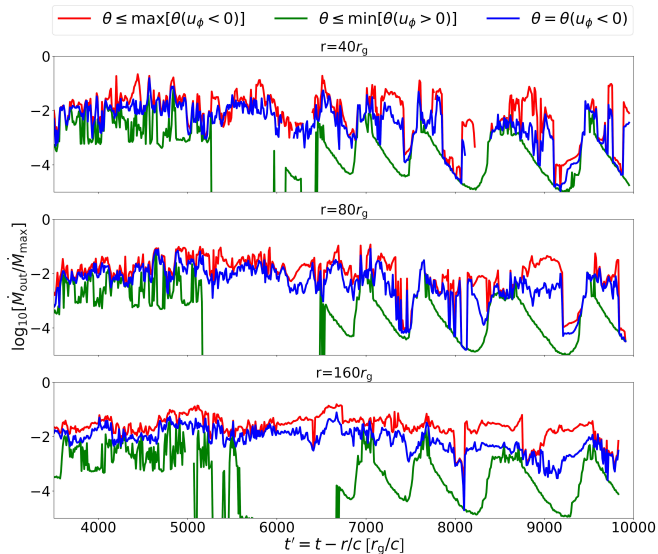


Figure D1. For spin parameter $a = -0.9375$, we compute the mass outflow rate \dot{M}_{out} in the jet at different radii (panels from top to bottom display $r/r_g = 40, 80$ and 160). The mass outflow rate is calculated using the tracer density, and adopting different definitions of the integration surface (see legend and text), all based on the fact that the jet has negative azimuthal four-velocity. The mass outflow rate is normalized to a representative horizon-scale mass accretion rate during phases of active accretion, which in code units is $\dot{M}_{\max} = 119.78$ (see Fig. 1(c)). Time is shifted in a radius-dependent way to account for light-travel time effects.

between the three different criteria suggests that the level of mass entrainment is strongly dependent on how the jet boundary is defined, with variations up to two orders of magnitude. While the red line is roughly consistent with the estimate by Wong et al. (2021), the green line is systematically lower by roughly one order of magnitude. Our results then can be reconciled with Wong et al. (2021) if most of the baryons entering the jet surface (identified by the red line) remain confined near the jet boundary, while the jet spine—carrying most of the electromagnetic flux—remains baryon-poor.

APPENDIX E: PASSIVE-TRACER FRACTION (χ_{tr}) MAPS

In the main text, most of our diagnostics are based on σ_{tr} (Figs. 2–4 and 5), which depends only on the magnetic field strength and on the physical baryon density supplied by the disk. As such, it is independent of the *ad hoc* numerical mass injection adopted for stability in low-density regions. For completeness, we present here the spatial structure of the tracer fraction χ_{tr} .

Figures E1, E2, and E3 show the spatial distribution of the tracer fraction χ_{tr} for the snapshots presented in Figs. 2, 3, and 4, while Fig. E4 presents the χ_{tr} analogue of Fig. 5. Because χ_{tr} is restricted to the interval $[0, 1]$, the lower bound of ~ -40 on the logarithmic colour scale simply corresponds to $\chi_{\text{tr}} = 0$ (i.e., no baryons). In these maps, any colour deviating from dark red (which corresponds to $\chi_{\text{tr}} = 1$) indicates that a fraction of the local mass density originates from numerical density injection. The χ_{tr} maps therefore provide a visual measure of how much numerical mass injection has occurred and where the numerically-injected mass has been transported. Regions that remain uniformly dark red consist entirely of disk-originated plasma, whereas blue or cyan patches mark locations affected by numerical mass injection. These diagnostics help interpret the σ_{tr} structure discussed in the main text in terms of the underlying tracer-fraction composition.

This paper has been typeset from a $\text{\TeX}/\text{\LaTeX}$ file prepared by the author.

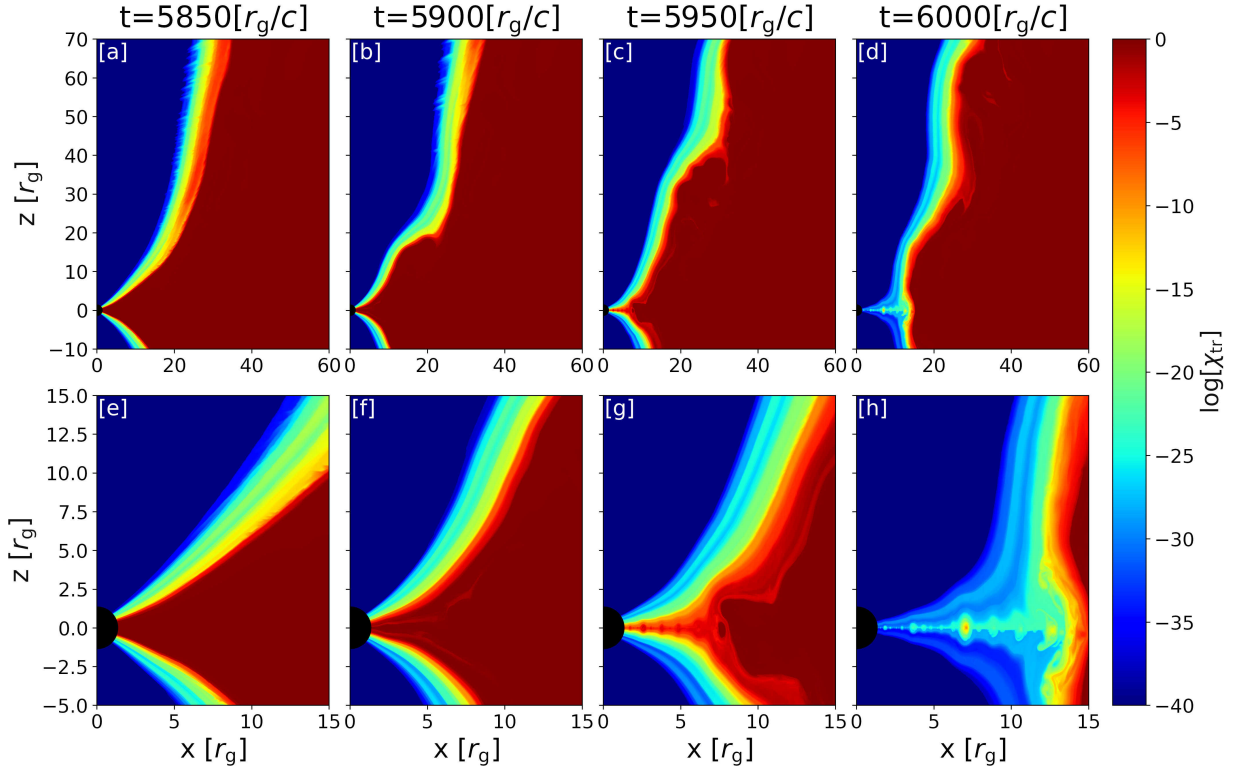


Figure E1. Same as Fig. 2 for the prograde case, but plotting the logarithm of the tracer fraction χ_{tr} .

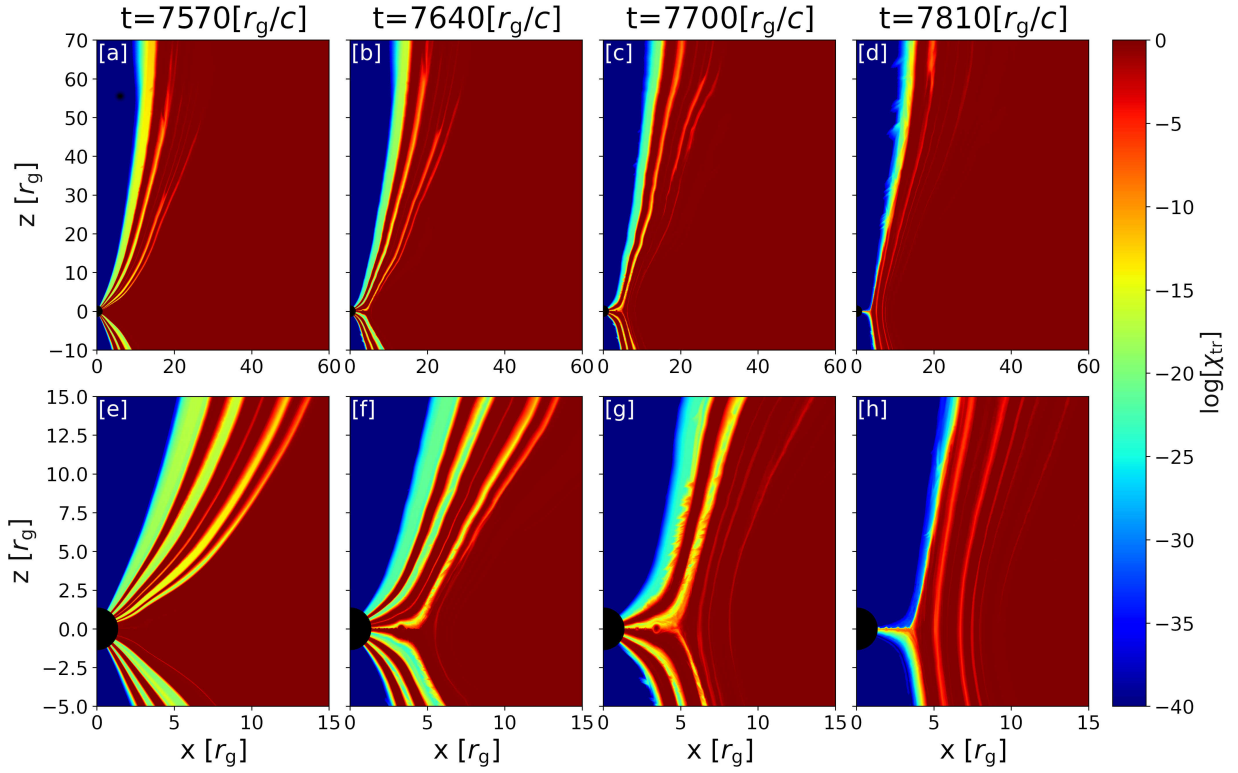


Figure E2. Same as Fig. 3 for the non-rotating case, but plotting the logarithm of the tracer fraction χ_{tr} .

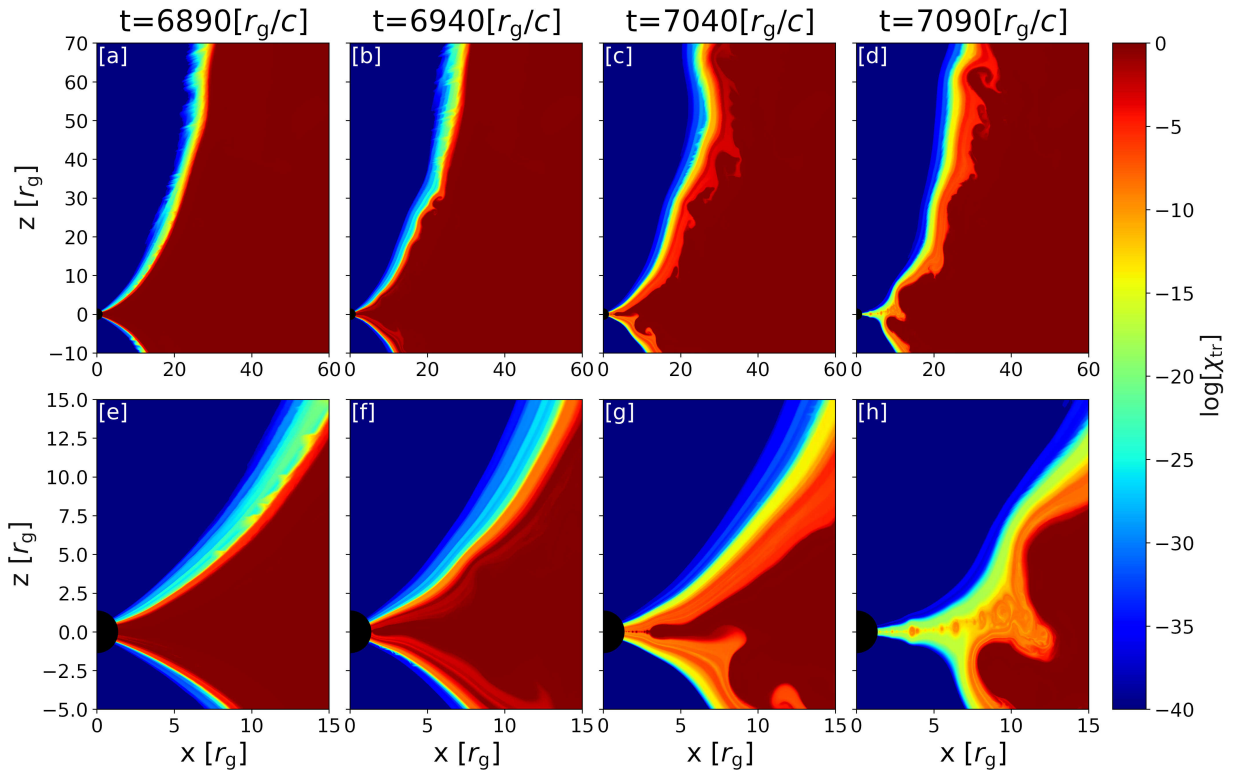


Figure E3. Same as Fig. 4 for the retrograde case, but plotting the logarithm of the tracer fraction χ_{tr} .

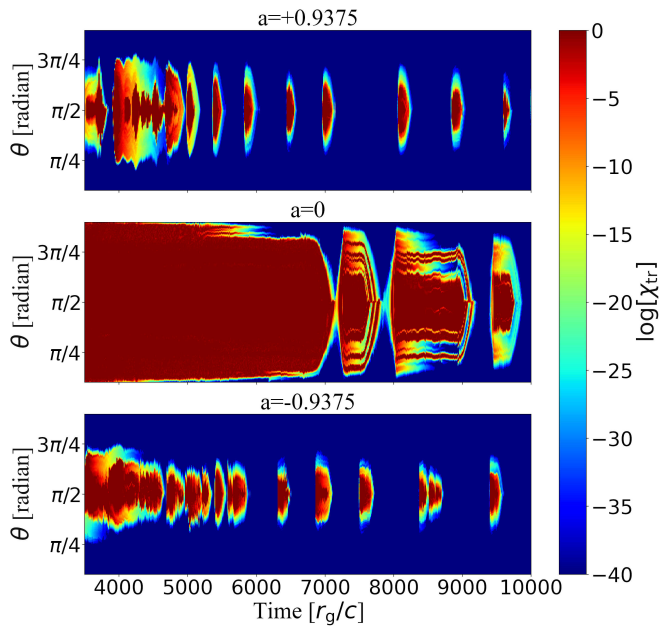


Figure E4. Same as Fig. 5, but plotting the logarithm of the tracer fraction χ_{tr} .